



HAL
open science

A microstructure-based three-scale homogenization model for predicting the elasto-viscoplastic behavior of duplex stainless steels

Eyram Tsekpuia, Adrien Guery, Nathalie Gey, Stéphane Berbenni

► To cite this version:

Eyram Tsekpuia, Adrien Guery, Nathalie Gey, Stéphane Berbenni. A microstructure-based three-scale homogenization model for predicting the elasto-viscoplastic behavior of duplex stainless steels. *International Journal of Plasticity*, 2023, 164, pp.103575. 10.1016/j.ijplas.2023.103575 . hal-04025423

HAL Id: hal-04025423

<https://hal.univ-lorraine.fr/hal-04025423>

Submitted on 12 Mar 2023

HAL is a multi-disciplinary open access archive for the deposit and dissemination of scientific research documents, whether they are published or not. The documents may come from teaching and research institutions in France or abroad, or from public or private research centers.

L'archive ouverte pluridisciplinaire **HAL**, est destinée au dépôt et à la diffusion de documents scientifiques de niveau recherche, publiés ou non, émanant des établissements d'enseignement et de recherche français ou étrangers, des laboratoires publics ou privés.

A microstructure-based three-scale homogenization model for predicting the elasto-viscoplastic behavior of duplex stainless steels

Eyram Tsekpuia ¹, Adrien Guery ², Nathalie Gey ¹, Stéphane Berbenni ^{1*}

¹Université de Lorraine, CNRS, Arts et Métiers ParisTech, LEM3, F-57000 Metz, France

²EDF Lab Les Renardières, Materials and Mechanics of Components department, F-77818 Moret-sur-Loing, France

Abstract

A new microstructure-informed three-scale homogenization scheme for elasto-viscoplastic heterogeneous materials is developed. It is applied to predict the mechanical behavior cast duplex austenitic-ferritic (AF) steels, which are widely used in primary loop of pressurized water reactors (PWR). At the first scale (microscale), the elasto-viscoplastic behavior of single crystals for both phases is modeled using linear elasticity and a viscoplastic crystal plasticity model. An “affine” type formulation based on the first moments of stresses is applied to the inelastic non-linear part of the deformation. Then, at the second scale (mesoscale), an EBSD-informed two-phase austenite/ferrite laminate structure (LS) model is developed with {110}-type habit planes (HP) in ferrite and a Kurdjumov-Sachs orientation relationship (KS-OR) between both phases. At the third scale (macroscale), the model considers a single ferritic primary grain as an aggregate of spherical two-phase laminate structure domains corresponding to the 24 KS-OR variants. The elasto-viscoplastic self-consistent scheme (EVPSC) is used through the Translated Fields (TF) method to obtain the effective behavior at this scale. The TF-EVPSC scheme is also used for an ensemble of primary ferritic grains to identify materials parameters from experimental tensile curves corresponding to as received and aged specimen. From EBSD measurements, the crystallographic data are thoroughly analyzed to physically feed the three-scale model. The results are discussed in terms of stress/strain responses in ferrite and austenite, which are correlated to the different KS-OR variants and HP orientations. The effect of primary ferritic grain crystallographic orientation and aging is also studied regarding monotonic and cyclic tests to study the possible origins of backstress in this material.

Keywords: A. Microstructures; EBSD; Homogenization; Crystal plasticity; Duplex steels; Elasto-viscoplastic material

*Corresponding author.

E-mail address: Stephane.Berbenni@univ-lorraine.fr

1. Introduction

To understand and predict the mechanical behaviors of multiphase and polycrystalline materials with complex microstructures, advanced micromechanical models need to be developed not only considering macroscopic fields (stresses and strains) but also fields in the different phases. Among these materials, cast duplex stainless steels are widely used in nuclear power plants in the primary loop of the cooling system of pressurized reactors (PWR) due to their good corrosion resistance and their superior mechanical properties (yield stress, ductility) (Solomon and Devine, 1982; Bonnet et al., 1990; Bethmont et al., 1996; Charles, 2009). These two-phase polycrystalline steels are constituted of a α -phase (ferrite) with volume fractions generally varying from 5% to 25% and a γ -phase (austenite). They exhibit a large yield stress due to the presence of body-centered cubic ferrite (b.c.c. crystal structure, the “hard phase”), while ductility is ensured thanks to the presence of face-centered cubic austenite (f.c.c. crystal structure, the “soft phase”). However, during in service behavior at about 300°C and aging during long periods of time (e.g. 10000h), while the mechanical behavior of austenite is not affected, ferrite may exhibit embrittlement and material’s fracture toughness decreases (Bonnet et al., 1990; Devillers-Guerville, 1998; Magnin and Moret, 1982; Trautwein and Gysel, 1982; Le Delliou and Sallet, 2015). Indeed, a spinodal decomposition of the ferrite α -phase (Fe-Cr solid solution) into α' -phase (Cr-rich phase) and α -phase (Fe-rich phase) occurs during aging besides a G-phase precipitation (Auger et al., 1990; Pareige et al., 2015; Badyka et al., 2019). Therefore, the damage mode of ferrite is modified and changes from ductile to brittle fracture due to cleavage cracking. The cleavage mode was observed to be controlled by tensile stresses (Bugat, 2000, Bugat et al. 2001; M’Cirdi, 2000; M’Cirdi et al. 2001). Therefore, good estimates of these stresses in both phases and especially in the ferritic phase are needed for as received and aged materials. Furthermore, the stress/strain responses of cast duplex stainless steels are strain rate sensitive as shown by the experimental cyclic responses (Bugat, 2000), which needs the development of a multiscale elasto-viscoplastic model.

Internal stresses in these materials were studied by Verhaeghe et al. (1996) identifying their sources directly from Bauschinger tests for aged and non-aged materials. Damage and fracture mechanisms were studied using TEM by Verhaeghe et al. (1997), X-Ray diffraction methods by M’Cirdi et al. (2001) and SEM with field measurements by Bugat et al. (2001). In a cast aged duplex stainless steel, a crystallographic cleavage criterion, based on a stress normal to a {100} plane in ferrite was reported by M’Cirdi et al. (2001). More recently, in situ synchrotron and neutron diffractions were

used to study the evolution of lattice strains in duplex steels during a tensile test and the occurrence of damage in the ferrite (Baczanski et al. 2016).

New experimental in-situ DIC (Digital Image Correlation) and EBSD (Electron Back Scattered Diffraction) based methods developed by Mollens (2022a) and Mollens et al. (2022b,c) reveal the heterogeneous deformation and micro-texture complexities, which motivates the development of new EBSD-informed microstructure-based multiscale homogenization model for predicting the elasto-viscoplastic behavior of duplex stainless steels. The microstructure heterogeneities are related to microstructure genesis and local correlations arise due to orientation relationships (OR). For duplex stainless steels, different orientation relationships were reported in the literature (Haghdadi et al., 2018; Mollens et al., 2022b). Most important observed ones are the Kurdjumov-Sachs (KS), Pitsch (P) and Nishiwama-Wassermann (NW). This microstructure genesis can also be simulated by advanced phase field models (PFM), considering the KS-OR from ferrite to austenite (Song et al., 2016). From the mechanical ground, full field crystal plasticity models based on Finite Element modeling (CPFEM) are good candidates to predict internal stress and strain fields at the microstructure level of complex microstructures (see e.g. Roters et al., 2010; Dodla et al., 2015; Li et al., 2019; Flipon et al., 2020; Kasemer and Dawson, 2020). However, they are still time consuming for the industrial applications. Analytical homogenization-based models remain relevant because they are less time consuming but need to be adapted to more complex microstructures than single phase polycrystalline structures using multiple scale transition methods.

Regarding micromechanical mean-field homogenization models for duplex steels, simple approximations using the simple Taylor (1938)'s model were reported by Verhaeghe (1996) and M'Cirdi (2000). The first self-consistent model for two-phase austenite/ferrite steels was due to Weng (1990), who used the Berveiller-Zaoui's (1979) self-consistent model. In this model, ferritic and austenitic grains were supposed to be spherical, which appears to be too simplistic for the present microstructure and isotropic secant moduli were only used for proportional loadings. A second numerical model was developed by Sigmund et al. (1995), who also considered a simple modeling assuming an aggregate of both phases with similar shapes. The Cailletaud-Pilvin's "Beta model" (Cailletaud, 1992; Cailletaud and Pilvin, 1994; Coudon et al., 2019) was used to describe the elastic-plastic responses of duplex stainless steels under non-proportional and cyclic loadings (Evrard et al., 2008, 2010). The Berveiller-Zaoui's self-consistent model was also used in combination with a physical intra-granular backstress formulation by Fournier et al. (2011) for predicting the high temperature cyclic behavior of martensitic steels. Baczanski et al. (2016) used synchrotron and neutron diffraction measurements to calibrate materials parameters in an elasto-plastic self-consistent scheme (EPSC) considering damage in duplex steels.

However, in all these above models, only two scales were considered in the scale transition of the micromechanical model between the phases and the aggregates. Later, Bugat et al. (1999) and Bugat (2000) developed for the first time a three-scale model based on the mean field “Beta model”, with two stress interaction laws for these duplex steels. An intermediate mesoscale was introduced, which was called “bi-crystal” by these authors. However, this model was only developed for isotropic elasticity, and, needed to be calibrated with full field FE unit cell calculations. The model was based on the EBSD data acquired in the 2000’s, and three different physical scales were essentially identified (Bugat et al. 1999; Bugat, 2000). Another interesting approach corresponding to multiple scale modeling of the local correlation between phases for purely anisotropic viscoplastic complex microstructures can be found in Lebensohn and Canova (1997), Lebensohn (1999), where the viscoplastic self-consistent scheme (VPSC) was extended to consider two-site interactions and lamellar structures in titanium aluminides (TiAl). For the same material, but considering a different modeling approach, Roos et al. (2004) developed a modeling approach based on a three-scale model using the Transformation Field Analysis (TFA) for plasticity together with the elastic self-consistent solution and lamellar phases. Kowalczyk-Gajewska (2011) developed a micromechanical model of polycrystalline materials with lamellar substructure in the framework of the Hill’s EPSC model (Hill, 1965) to study the elastic anisotropies and the initial yield surfaces for polycrystalline microstructures of Ti-Al. Franciosi and Berbenni (2007, 2008) also developed a multi-scale sequential multi-laminate model based on a non-uniform TFA approach with “affine” type approximation to describe the evolution of heterogeneous plastic domains in metallic polycrystals. Stress/strain estimates were improved at the macroscopic and at the grain levels, as compared to classic EPSC scheme, which assumes piece-wise uniform plastic strains in grains. The lamellar-based approach of Lebensohn et al. (1997,1999) was recently applied to a Ti-6Al-4V alloy to accurately model the local crystallographic correlations in such complex multiscale microstructures (Riyad et al., 2021). A finite strain lamellar-based model elasto-viscoplastic model was developed by Uchida and Tada (2013) and was applied to semi-crystalline polymers. Another lamellar-based approach was used in a multi-scale model (Maresca et al., 2014) to describe the micromechanical behavior of martensitic steels. In their approach, martensitic blocks were seen as a two-phase layered composite material with martensitic laths and retained austenite interlayer.

Therefore, we propose here to extend the EVPSC (Elasto-Visco-Plastic Self-Consistent) scheme based on the “Translated Field” (TF) method with “affine” type linearization of the viscoplastic flow rule as developed by Mareau and Berbenni (2015), for such duplex steels with complex microstructure. This advanced EVPSC scheme was successfully applied to near- β titanium alloys in Lahdi et al. (2018, 2020). While the original approach based on the TF method of Paquin et al.

(1999, 2001) was derived from a classical “secant” approximation, this work adopts the first order “affine” linearization (see e.g. Masson et al., 2000; Doghri et al., 2010) of the viscoplastic flow rule, i.e. a first order Taylor expansion of the viscoplastic strain rate at the microscale. It has been observed in Mareau and Berbenni (2015) that the first order “affine” formulation yields softer responses than the secant formulation for different elasto-viscoplastic polycrystals during monotonic and cyclic loadings. Other EVPSC approaches using the “additive interaction law” (Molinari et al., 1997; Mercier and Molinari, 2009) were adapted for polycrystals with “affine” type approximation at large strains (Wang et al., 2010; Zecevic et al. 2020). Another numerically efficient “affine” type EVPSC scheme was also recently derived by Jeong and Tomé (2020) and applied to steels subjected to loading path changes. According to Mercier et al. (2012), Berbenni and Capolungo (2015) and Mareau and Berbenni (2015), the use of the first order “affine” formulation improves the estimate of the effective behavior, in comparisons with full-field calculations (FEM, FFT), even when the viscoplastic flow rule is highly nonlinear. Homogenization methods for elasto-viscoplastic composite materials considering field statistics, i.e. second moments of stresses, were derived (see e.g. Lahellec and Suquet, 2007, 2013; Brassart et al., 2012; Wu et al., 2017; Masson et al., 2020; Berbenni, 2021). A recent modeling approach for elasto-viscoplastic polycrystals based on a differential variational procedure (Das and Ponte Castañeda, 2020) further improves the numerical results compared to FFT full field results. However, it needs a more complex numerical treatment of cyclic and non-proportional loadings, which has not been solved yet.

Following the recent findings and EBSD analyses of Mollens et al. (2022b,c), a multiscale modeling strategy accounting for the relevant scales must be considered when dealing with the complex microstructure of austenite-ferritic (duplex) steels. In the present paper, a new microstructure-based three-scale homogenization model including two scale transitions will be developed and discussed. The paper is organized as follows. In section 2, the duplex stainless steel is presented. The chemical composition, the microstructure and the tensile mechanical properties are reported. In addition, an EBSD analysis is proposed to identify the different crystallographic orientations and the heterogeneities in the microstructure. In section 3, the micromechanical model based on a three-scale analytical homogenization-based method for elasto-viscoplastic heterogeneous materials is developed and specifically applied to duplex stainless steels. In section 4, the results of the model are presented at different scales denominated micro-, meso-, and macro-scales. The strain/stress fields in both phases are predicted for the different KS-OR variants, which are present in the primary ferritic grains. The effects of ferrite grain orientations and aging are numerically studied. The different internal stresses present in the microstructure are analyzed in the light of this new approach through cyclic loading responses and a backstress analysis.

2. Material

2.1. Microstructure and mechanical properties

The material of interest is a CF8M alloy (AFNOR Z3CND1910), which is representative of cast duplex stainless steels used in the primary loop components of Pressurized Water Reactors (PWR) in France. Its chemical composition is given in Table 1. Its microstructure has been characterized by EBSD in the previous study of Mollens (2022a), see Figure 1. It is made of primary polygonal ferritic grains of 200 to 1000 micrometers partially transformed with respect of an orientation relationship into Widmanstätten austenite laths of 10 to 50 micrometers width. The retained ferrite phase accounts for about 25% of the total volume fraction. It is located between the austenite laths. Here, only the cast microstructure will be thoroughly modeled, but we will discuss the prospective effect of aging by considering a higher flow stress for ferrite, which may be due to precipitation during aging.

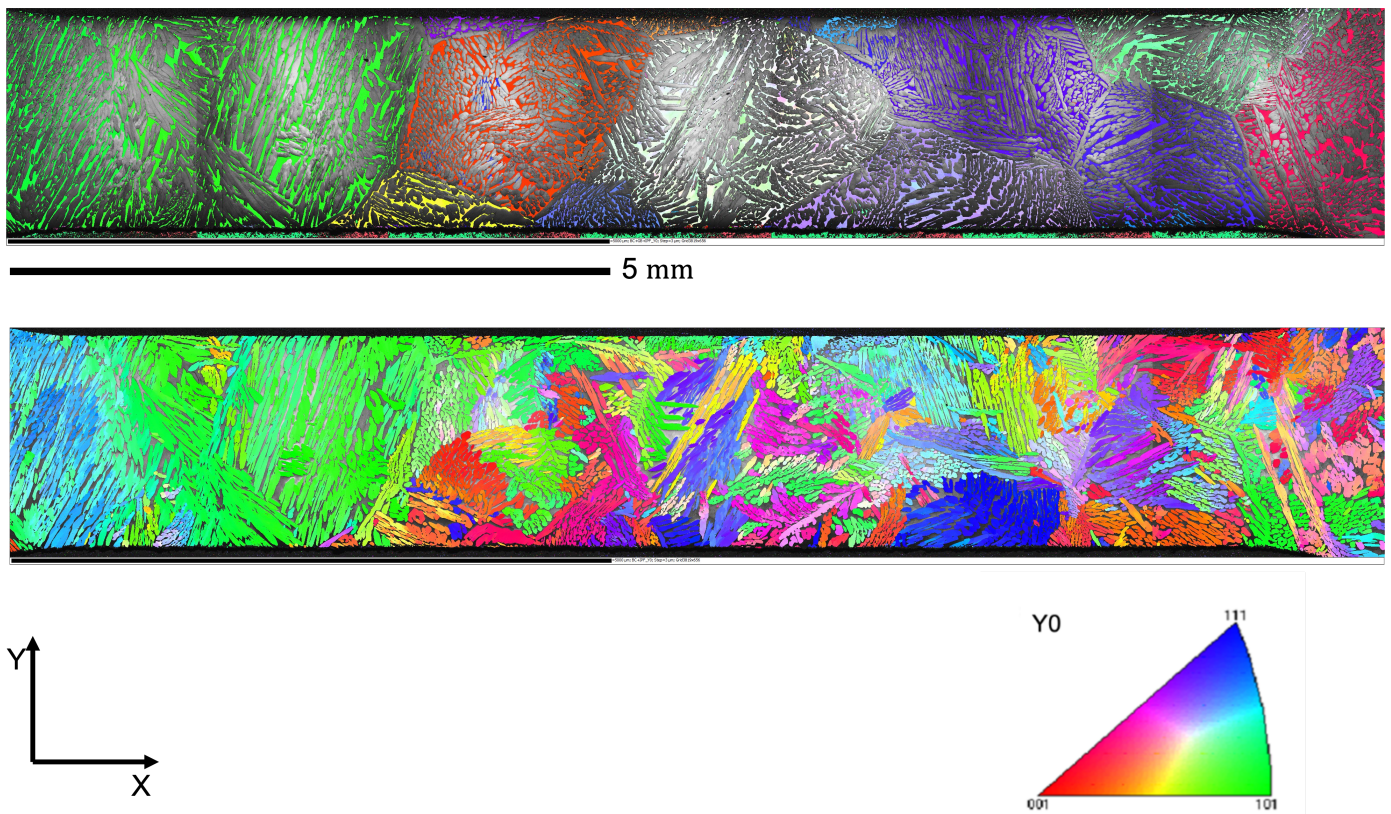


Figure 1. Inverse Pole Figure map//Y of the as-cast duplex steel respectively for retained ferrite (upper map) and austenite (bottom map) using EBSD data from Mollens (2022a).

Table 1. Chemical composition of the studied CF8M material from Mollens et al. (2022c).

Element	C	Mn	Si	Ni	Cr	Mo	S	P
Content (%wt)	0.032	0.80	1.04	10.4	20.9	2.68	0.0007	0.025

The mechanical behavior of the material at the as-received state and after thermal aging at 350°C during 1000h has been characterized by Mollens (2022a) with tensile tests using normalized TC6 specimens. The resulting tensile curves are shown in Figure 2. Thermal aging induces a small increase of the yield stress, an increase of the ultimate tensile stress and a decrease of the elongation at fracture, consistent with previous studies (Bugat, 2000; Michaud et al., 1994).

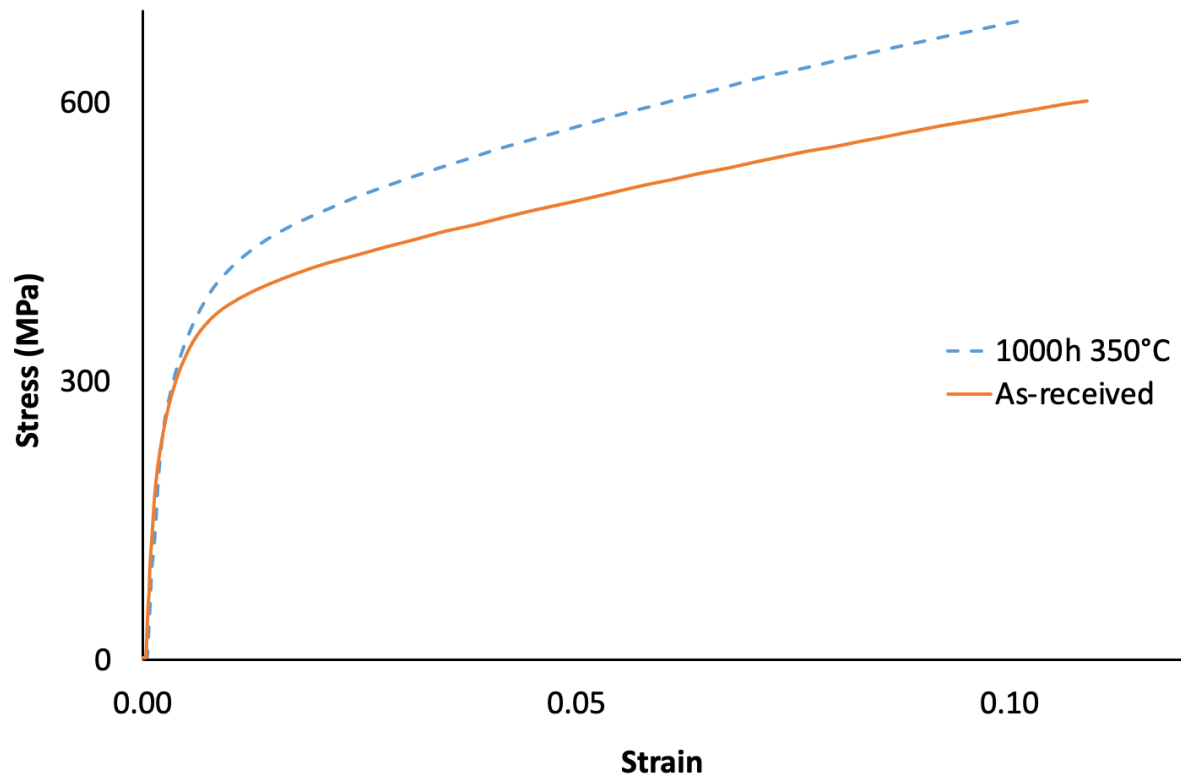
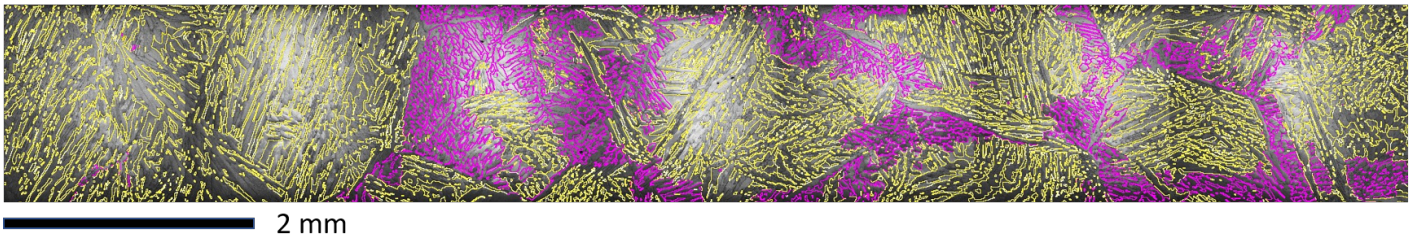


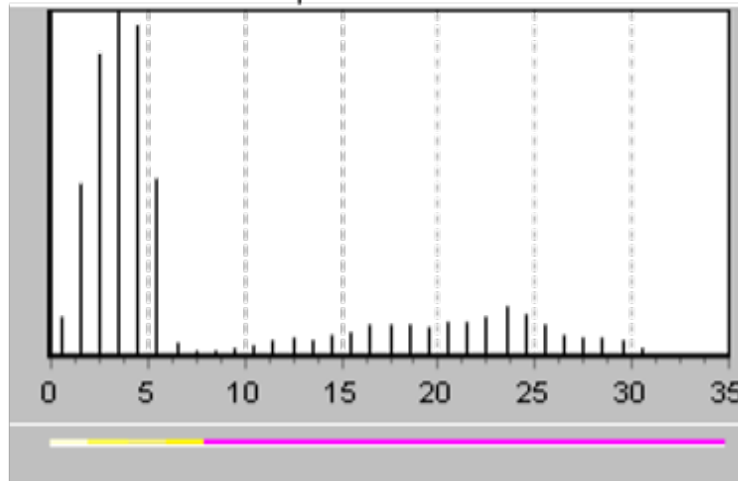
Figure 2. Tensile behavior (true stresses/ true strains) measured at ambient temperature on the studied material at the as-received state and aged 1000h at 350°C (Mollens, 2022a).

2.2. Crystallographic and morphological features of the microstructure

EBSD data shown in Figure 1 were first analyzed to characterize the local orientation correlations between both ferrite/austenite phases. Figure 3 displays the local deviation from KS-OR at the ferrite/austenite interfaces. The duplex microstructure was found to display a significantly higher content of close KS-OR interfaces, which are represented with white and yellow interfaces in Figure 3. However, no unique and strict orientation relationship exist between both phases, as already mentioned in a previous work (Mollens et al., 2022b). Moreover, close to some primary ferrite boundaries, the austenite phase exhibit no longer a lath-like morphology and no OR is observed. This happens mainly for austenite phase that have grown at each side of a primary ferrite grain with close orientation.



(a)



(b)

Figure 3. (a) EBSD map plotting the KS-OR deviation at the ferrite/austenite interfaces for as received cast material, and (b) the corresponding distribution with the angular deviation color code (in $^{\circ}$).

The EBSD data were further investigated to analyze the trace of ferrite/austenite interfaces respecting KS-OR. The result shows that most of the traces are consistent with a $\{110\}_{\alpha}$ plane of the primary ferrite grain, which acts as a habit plane (denoted HP in the following) in the reverse KS-OR (see an example in Figure 4).

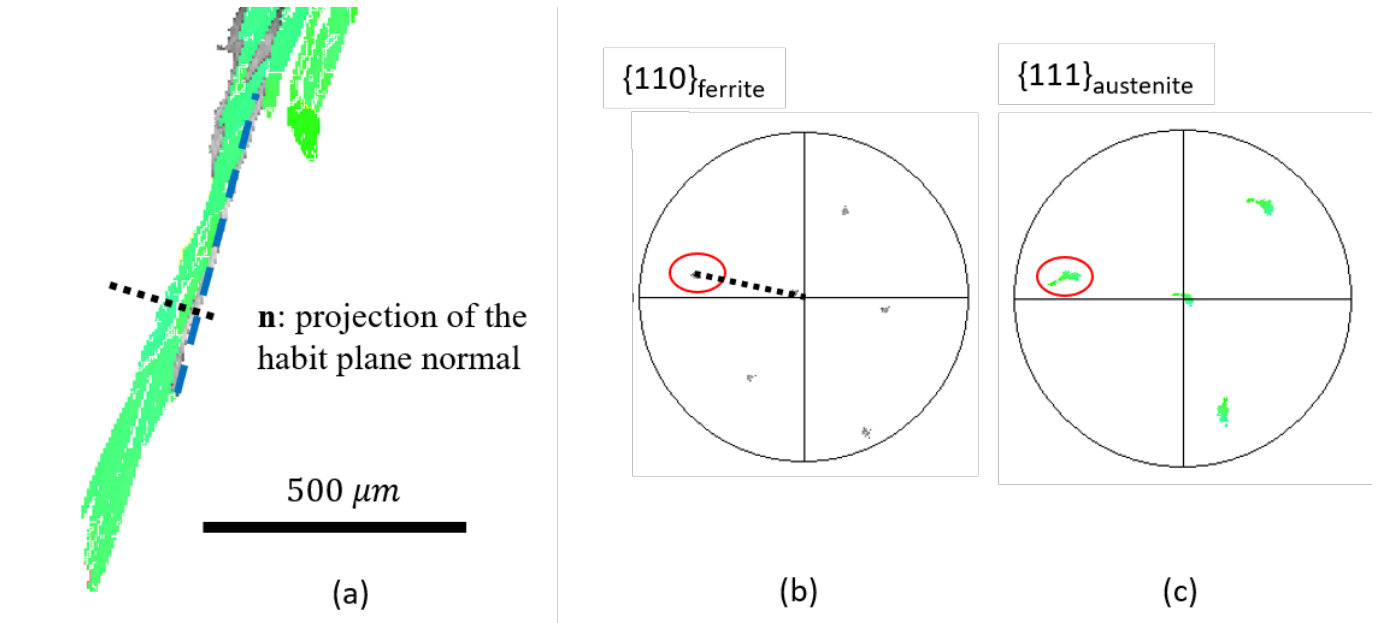


Figure 4. (a) Geometric definition of the habit plane (HP) with habit plane normal \mathbf{n} , (b) $\{110\}$ pole figure for ferrite, (c) $\{111\}$ pole figure for austenite.

Assuming close KS-OR for the ferrite to austenite transformation, Table 2 gives the 24 potential variants obtained from a primary ferrite grain (defined by the orientation (0,0,0) for ferrite). For each variant, the corresponding HP is indicated as well as the Bain group it belongs to. Packets of 4 variants sharing the same HP are identified by a similar color. Inside such a packet, the 4 variants belong 2 by 2 to two Bain domains.

Table 2. 24 KS variant definition for b.c.c. to f.c.c transformation according to the KS-OR. Color code means the HP's type (6 different habit planes). The variants are divided into 3 Bain groups, denoted B1 to B3. The list of the 24 group symmetry matrices to generate these variants is given in Table A.1, see Appendix A.

Variants	φ_1 ($^\circ$)	ϕ ($^\circ$)	φ_2 ($^\circ$)	HP plane (h k l)	HP direction [u v w]	HP name	Bain group
V1	5.77	48.19	5.77	(1 $\bar{1}$ 0)	[1 1 1]	H1	B1:x
V2	95.77	48.19	5.77	(1 1 0)	$\bar{1}$ 1 1]	H2	B2:y
V3:	185.77	48.19	5.77	($\bar{1}$ 1 0)	$\bar{1}$ $\bar{1}$ 1]	H1	B1:x
V4:	275.77	48.19	5.77	($\bar{1}$ $\bar{1}$ 0)	1 $\bar{1}$ 1]	H2	B2:y
V5:	6.41	137.87	14.39	(1 0 $\bar{1}$)	[1 $\bar{1}$ 1]	H3	B1:x
V6:	48.05	85.70	99.62	(1 0 1)	$\bar{1}$ $\bar{1}$ 1]	H4	B3:z
V7:	353.59	42.13	194.39	($\bar{1}$ 0 1)	$\bar{1}$ 1 $\bar{1}$]	H3	B1:x
V8:	311.95	94.30	279.62	($\bar{1}$ 0 $\bar{1}$)	[1 $\bar{1}$ $\bar{1}$]	H4	B3:z
V9:	96.41	137.87	14.39	(0 1 $\bar{1}$)	[1 1 1]	H5	B2:y
V10:	138.05	85.70	99.62	(0 1 1)	[1 $\bar{1}$ 1]	H6	B3:z
V11:	83.59	42.13	194.39	(0 $\bar{1}$ 1)	[1 $\bar{1}$ $\bar{1}$]	H5	B2:y

V12:	41.95	94.30	279.62	$(0 \bar{1} \bar{1})$	$[1 1 \bar{1}]$	H6	B3:z
V13:	186.41	137.87	14.39	$(\bar{1} 0 \bar{1})$	$[\bar{1} 1 1]$	H4	B1:x
V14:	228.05	85.70	99.62	$(\bar{1} 0 1)$	$[1 1 1]$	H3	B3:z
V15:	173.59	42.13	194.39	$(1 0 1)$	$[1 1 \bar{1}]$	H4	B1:x
V16:	131.95	94.30	279.62	$(1 0 \bar{1})$	$[\bar{1} 1 \bar{1}]$	H3	B3:z
V17:	276.41	137.87	14.39	$(0 \bar{1} \bar{1})$	$[\bar{1} \bar{1} 1]$	H6	B2:y
V18:	318.05	85.70	99.62	$(0 \bar{1} 1)$	$[\bar{1} 1 1]$	H5	B3:z
V19:	263.59	42.13	194.39	$(0 1 1)$	$[\bar{1} 1 \bar{1}]$	H6	B2:y
V20:	221.95	94.30	279.62	$(0 1 \bar{1})$	$[\bar{1} \bar{1} \bar{1}]$	H5	B3:z
V21:	174.23	131.81	185.77	$(1 1 0)$	$[1 \bar{1} \bar{1}]$	H2	B1:x
V22:	264.23	131.81	185.77	$(\bar{1} 1 0)$	$[1 1 \bar{1}]$	H1	B2:y
V23:	354.23	131.81	185.77	$(\bar{1} \bar{1} 0)$	$[\bar{1} 1 \bar{1}]$	H2	B1:x
V24:	84.23	131.81	185.77	$(1 \bar{1} 0)$	$[\bar{1} \bar{1} \bar{1}]$	H1	B2:y

2.3. Resulting physical scales and modeling assumptions: towards a three-scale homogenization model

Finally, from the analysis of the experimental EBSD data (Mollens et al., 2022b), four physical scales can be identified to describe the complex microstructure of the as received cast duplex steel. Figure 5 reports the microstructure with four identified physical scales from EBSD analysis, and the schematic principle of the three-scale homogenization model based on two scale transitions assuming that macro-homogeneity conditions are satisfied. The first physical scale is defined by the single crystalline austenite lath or ferrite interlayer, where classic crystal plasticity will be used in the model to describe the small strain viscoplastic behavior of both phases at the microscale. The austenite lath is characterized by a smooth orientation spread. This lath results from a displacive transformation according to a close $\{110\}_\alpha$ HP (i.e., a $\{110\}$ -type plane in ferrite, see Table 2) and respecting closely the KS-OR with the surrounding ferrite grain. The second physical scale is dictated by a cluster of adjacent austenite laths, characterized by constrained morphological and crystallographic parameters. In a cluster, the austenite laths often share the same orientation with an increased orientation spread. They are separated by layers of primary ferrite. In this contribution, this cluster is modeled at the mesoscale with a two-phase laminate structure (LS) homogenization model. The LS model will be used as scale transition rule from microscale to mesoscale, see Figure 5. The normal vector to the interface between both phases in the cluster is of $[110]_\alpha$ type (i.e., a $[110]$ -type direction in the crystal ferrite frame). The third physical scale is defined by the primary ferritic grain that contains all the austenite lath clusters. We can notice that adjacent lath clusters often include two austenite variants belonging to the same Bain group. We will consider all the possible 24 KS-OR variants in the modeling. Finally, the fourth physical scale is defined as an ensemble of primary ferritic grains. Here, the EVPSC scheme based on the Translated Field (TF) method will be used as scale transition rule from mesoscale to macroscale with different representative volume elements (RVE) defined as a single primary ferritic grain (third physical scale)

or as an ensemble of primary ferritic grains (fourth physical scale), see Figure 5. The crystal plasticity parameters of the three-scale model will be calibrated from experimental tensile curves considering an ensemble of 15 primary ferritic grains (see Table A.2 in Appendix A).

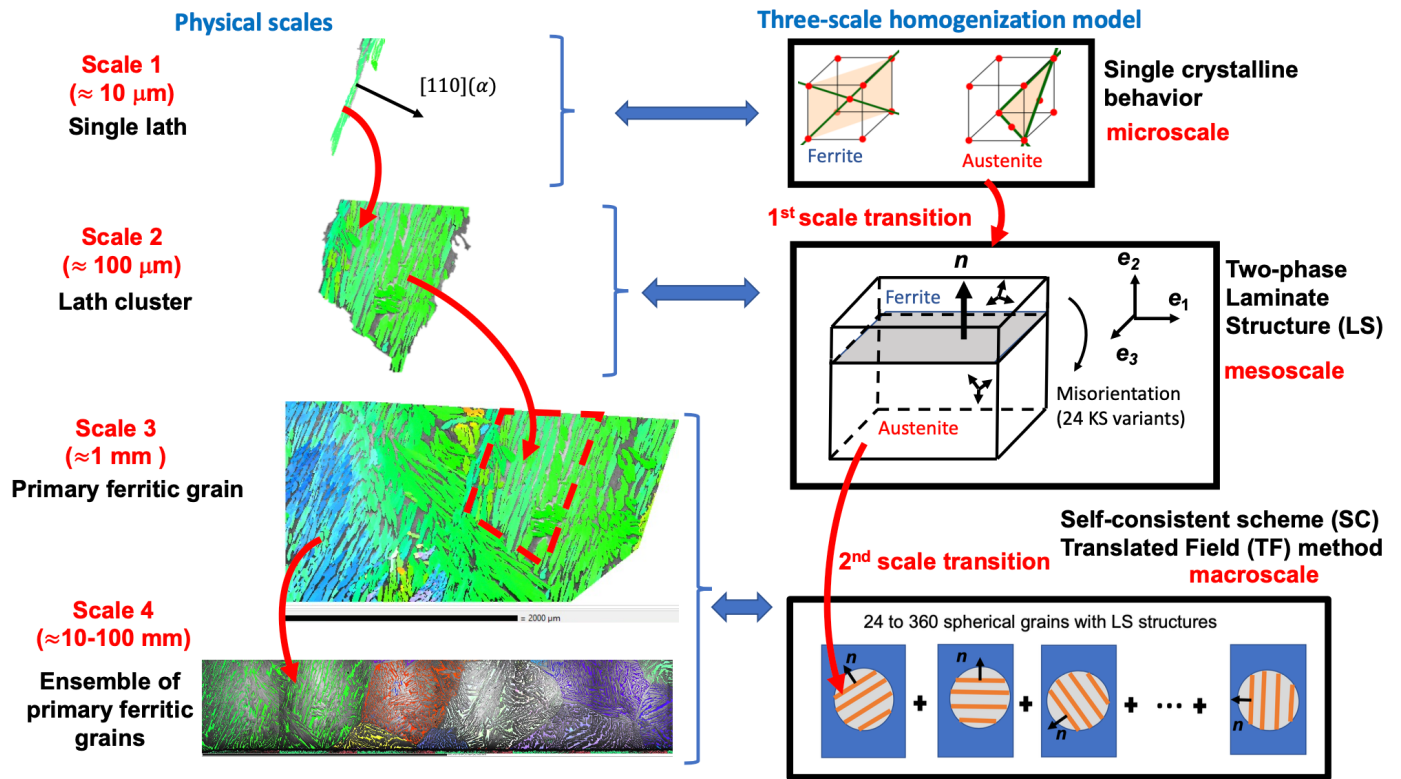


Figure 5. Description of the microstructure with four identified physical scales inferred from the present EBSD analysis with the presence of lath clusters inside primary ferritic grains (left); Schematic principle of the three-scale homogenization model based on two scale transitions (right): from microscale to mesoscale with the two-phase LS model, and, from mesoscale to macroscale with the SC scheme based on the TF method.

3. Three-scale model

The modeling of the elasto-viscoplastic behavior of duplex stainless steels is derived following the different scales and modeling assumptions reported in Figure 5. The TF-based EVPSC model is reconsidered with two homogenization steps in a three-scale model. The first step is a homogenization procedure for the two-phase (ferrite/austenite) LS considering an elasto-viscoplastic behavior at the microscale with “affine” type formulation for both phases. Stress and strain concentration equations allow to give an estimate of mean fields in both phases at the

microscale accounting for the stress/strain incompatibilities due to the presence of the HP. The homogenized properties of the LS obtained at this first step, i.e., at the mesoscale, will be incorporated in the TF-EVPSC scheme for the second homogenization procedure. This one considers at the macroscale an ensemble of two-phase LS constrained by spherical domains corresponding to the different KS-OR variants. The 24 variants (see Table 2) will be considered with equal volume fraction for each primary ferritic grain. Then, the macroscale model is built up with the homogenized elasto-viscoplastic behavior for one or 15 primary ferritic grains as reported in Table A.2 in Appendix A.

The computational flowchart of the three-scale homogenization model highlighting both scale transitions (TF-EVPSC scheme and LS-model) is reported in Figure 6, using the same notations as in the text (see next sections). For this homogenization model, the elasto-viscoplastic behavior with an “affine” type formulation is chosen and first reported in section 3.1. The meso- to macro- scale model using the TF-EVPSC scheme (see Figure 6) is detailed in section 3.2. Then, the micro- to meso- scale model based on the two-phase LS (see Figure 6) is detailed in section 3.3. Finally, the constitutive laws at the microscale for ferrite (denoted “ α ”) and austenite (denoted “ γ ”) (see Figure 6) are obtained from single crystal plasticity, as described in section 3.4. Boundary conditions at the different scales are derived from those at the macroscopic scale using the macro-homogeneity condition. We assume that the average fields in two-phase LS grains, obtained from stress and strain concentration equations derived from the TF-EVPSC serve as boundary conditions at the mesoscale assuming the homogeneity condition at this scale.

Throughout the development of the micromechanical model, scalar variables are represented in italic font, vectors in italic and bold font, rank 2 and 4 tensors in bold font. Annotations are represented in regular font. The symbol “ \cdot ” denotes the contracted product between two tensors. The symbols $\langle \cdot \rangle$ and $\langle \cdot \rangle^L$ denote the ensemble volume averages at the macroscale and the mesoscale, respectively. Indicial notations for tensor and vector components are used in Cartesian coordinates and are written in regular fonts to make a difference with other scalars. The Einstein’s summation convention is used.

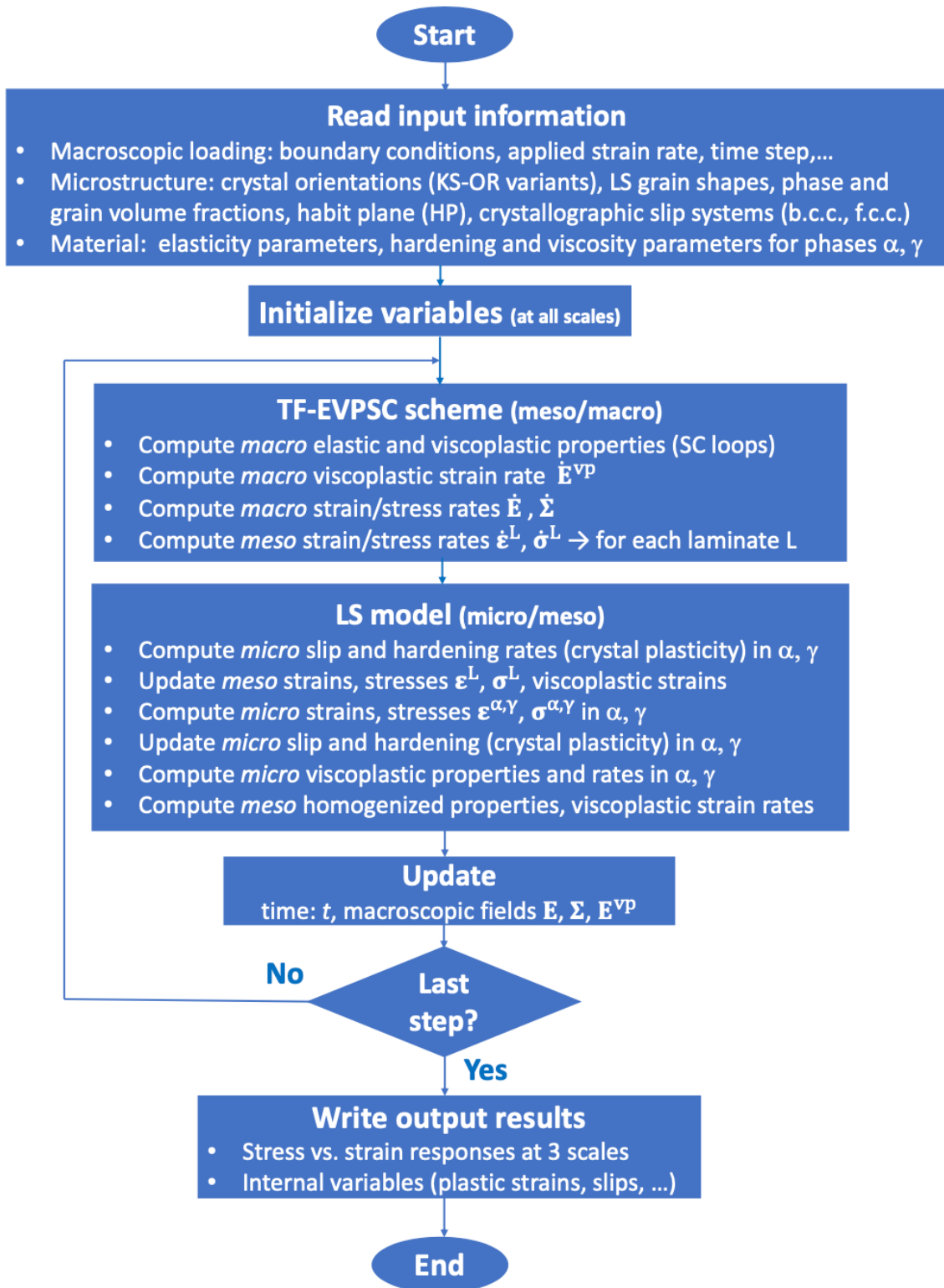


Figure 6. Flowchart of the developed three-scale elasto-viscoplastic homogenization model (see notations as in the text).

3.1. “Affine” type formulation

Within the infinitesimal strain framework, the total local strain rate tensor relative to an elasto-viscoplastic behavior of Maxwell type is decomposed into:

$$\dot{\boldsymbol{\varepsilon}} = \dot{\boldsymbol{\varepsilon}}^e + \dot{\boldsymbol{\varepsilon}}^{vp} \quad (1)$$

with $\dot{\boldsymbol{\varepsilon}}^e = \mathbf{s} : \dot{\boldsymbol{\sigma}}$ the elastic strain rate tensor obtained from the generalized Hooke's law, where \mathbf{s} ($= \mathbf{c}^{-1}$) is the local elastic compliance tensor, $\boldsymbol{\sigma}$ is the Cauchy stress tensor, and $\dot{\boldsymbol{\varepsilon}}^{vp} = \mathbf{g}(\boldsymbol{\sigma})$ is the nonlinear stress dependent constitutive law (plastic flow rule) to derive the viscoplastic strain rate tensor. It will be determined from the constitutive laws of single crystalline austenite laths and ferrite interlayer (see subsection 3.4). As performed in Mareau and Berbenni (2015), its first order "affine" linearization can be written as follows at a given reference stress:

$$\dot{\boldsymbol{\varepsilon}}^{vp} = \mathbf{g}(\boldsymbol{\sigma}) \approx \mathbf{m}_t : \boldsymbol{\sigma} + \dot{\boldsymbol{\eta}} \quad (2)$$

where \mathbf{m}_t is the tangent viscoplastic compliance tensor (with subscript "t" as "tangent") defined by:

$$\mathbf{m}_t = \frac{\partial \mathbf{g}(\boldsymbol{\sigma})}{\partial \boldsymbol{\sigma}} \quad (3)$$

and $\dot{\boldsymbol{\eta}}$ corresponds to the back-extrapolated viscoplastic strain rate tensor. The Cauchy stress tensor can also be expressed as a nonlinear tensorial function \mathbf{h} of $\dot{\boldsymbol{\varepsilon}}^{vp}$ and then could be written in its linearized form at a given reference viscoplastic strain rate as:

$$\boldsymbol{\sigma} = \mathbf{h}(\dot{\boldsymbol{\varepsilon}}^{vp}) \approx \mathbf{b}_t : \dot{\boldsymbol{\varepsilon}}^{vp} + \boldsymbol{\zeta} \quad (4)$$

where $\mathbf{b}_t = \mathbf{m}_t^{-1}$ is the tangent viscoplastic modulus tensor, $\boldsymbol{\zeta}$ is the back-extrapolated stress tensor related to the back-extrapolated viscoplastic strain rate: $\boldsymbol{\zeta} = -\mathbf{b}_t : \dot{\boldsymbol{\eta}}$. Therefore, the final linearized form of the elasto-viscoplastic constitutive law is:

$$\dot{\boldsymbol{\varepsilon}} = \mathbf{s} : \dot{\boldsymbol{\sigma}} + \mathbf{m}_t : \boldsymbol{\sigma} + \dot{\boldsymbol{\eta}} \quad (5)$$

3.2. Meso- to macroscale transition: TF-based EVPSC

In this paper, the scale transition from a single two-phase LS at the mesoscale to the macroscale (one primary ferritic grain or an ensemble of ferritic primary grains) is assessed through the Translated Field (TF) based EVPSC method with affine-type extension. This TF-EVPSC scheme was first developed in Mareau and Berbenni (2015) and more recently applied to polycrystalline β -Ti alloys by Lahdi et al. (2018, 2020).

At the macroscale, the average strain and stress rate tensors are defined by: $\langle \dot{\epsilon} \rangle = \dot{\mathbf{E}}$ and $\langle \dot{\sigma} \rangle = \dot{\mathbf{\Sigma}}$, while at the mesoscale, the average strain and stress rate tensors for each laminate structure (LS) denoted “L” are defined by: $\dot{\epsilon}^L = \langle \dot{\epsilon} \rangle^L$ and $\dot{\sigma}^L = \langle \dot{\sigma} \rangle^L$. Then, the average elastic strain rate tensor in each “L” is given by the linear elastic Hooke’s law: $\dot{\epsilon}^{eL} = \mathbf{s}^L : \dot{\sigma}^L$, and, the viscoplastic strain rate tensor is formulated using an affine type approximation: $\dot{\epsilon}^{vpL} \approx \mathbf{m}_t^L : \dot{\sigma}^L + \dot{\eta}^L$, or, $\dot{\sigma}^L \approx \mathbf{b}_t^L : \dot{\epsilon}^{vpL} + \zeta^L$, see equations (2-5).

In the TF-EVPSC (Mareau and Berbenni, 2015; Lhadi et al. 2018), the strain rate concentration law gives the strain rate tensor $\dot{\epsilon}^L$ in each LS for an applied macroscopic strain rate tensor $\dot{\mathbf{E}}$:

$$\begin{aligned} \dot{\epsilon}^L = & \mathbf{A}^C : \dot{\mathbf{E}} + \mathbf{A}^C : \Gamma_1^{Bt} : (\mathbf{b}_t^L : \dot{\eta}^L + \mathbf{B}_t : \dot{\mathbf{N}}) + \mathbf{A}^C : \Gamma_1^C : (\delta \mathbf{c}^L : \dot{\epsilon}^{vpL} + \mathbf{c}^L : \mathbf{A}^C : (\langle \dot{\epsilon}^{vp} \rangle - \dot{\mathbf{E}}^{vp})) - \\ & \mathbf{A}^C : \Gamma_1^{Bt} : (\delta \mathbf{b}_t^L : \dot{\epsilon}^{vpL} - \mathbf{b}_t^L : \mathbf{A}^{Bt} : (\mathbf{M}_t : \dot{\mathbf{\Sigma}} + \dot{\mathbf{N}} - \langle \dot{\epsilon}^{vp} \rangle)) + \mathbf{A}^C : (\Gamma_1^C : \mathbf{C} - \Gamma_1^{Bt} : \mathbf{B}_t) : (\dot{\epsilon}^{vpL} - \mathbf{A}^{Bt} : \langle \dot{\epsilon}^{vp} \rangle) - \\ & \mathbf{A}^C : (\Gamma_1^C : \mathbf{C} - \Gamma_1^{Bt} : \mathbf{B}_t) : (\mathbf{A}^{Bt} : \Gamma_1^{Bt} : (\mathbf{b}_t^L : \dot{\eta}^L - \mathbf{B}_t : \dot{\mathbf{N}})) \end{aligned} \quad (6)$$

where $\dot{\mathbf{E}}^{vp}$ is the macroscopic viscoplastic strain rate defined later in equation (11) (it is noteworthy that is different from $\langle \dot{\epsilon}^{vp} \rangle$). In equation (6), the effective elastic and viscoplastic moduli, \mathbf{C} and \mathbf{B}_t , are given by one site Self-Consistent (SC) scheme iteration loops with a fixed-point algorithm:

$$\mathbf{C} = \langle \mathbf{c}^L : \mathbf{A}^C \rangle : \langle \mathbf{A}^C \rangle^{-1} \quad (7a)$$

$$\mathbf{B}_t = \langle \mathbf{b}_t^L : \mathbf{A}^{Bt} \rangle : \langle \mathbf{A}^{Bt} \rangle^{-1} \quad (7b)$$

In equation (6), $\Gamma_1^C : \mathbf{C}$, $\Gamma_1^{Bt} : \mathbf{B}_t$ denote the Eshelby tensors (Eshelby, 1957) associated to \mathbf{C} and \mathbf{B}_t , with $\Gamma_1^{C \text{ or } Bt}$ the local parts of the modified Green tensors (Kröner, 1990). The 4th rank elastic and viscoplastic strain concentrations tensors denoted \mathbf{A}^C , \mathbf{A}^{Bt} are given by $\mathbf{A}^C = (\mathbf{I} + \Gamma_1^C : \delta \mathbf{c}^L)^{-1}$, $\mathbf{A}^{Bt} = (\mathbf{I} + \Gamma_1^{Bt} : \delta \mathbf{b}_t^L)^{-1}$ respectively, with \mathbf{I} the fourth order unit tensor, $\delta \mathbf{b}_t^L = \mathbf{b}_t^L - \mathbf{B}_t$, $\delta \mathbf{c}^L = \mathbf{c}^L - \mathbf{C}$.

The effective back-extrapolated strain rate $\dot{\mathbf{N}}$ in equation (6) is obtained from:

$$\mathbf{B}_t : \dot{\mathbf{N}} = \langle \mathbf{b}_t^L : \dot{\eta}^L - \mathbf{b}_t^L : \mathbf{A}^{Bt} : \Gamma_1^{Bt} : (\mathbf{b}_t^L : \dot{\eta}^L - \mathbf{B}_t : \dot{\mathbf{N}}) \rangle \quad (8)$$

Then, from equation (8):

$$\dot{\mathbf{N}} = \mathbf{M}_t : (\langle \mathbf{b}_t^L : \mathbf{A}^{B_t} : \Gamma_1^{B_t} \rangle - \mathbf{I})^{-1} : \langle \mathbf{b}_t^L : \mathbf{A}^{B_t} : \Gamma_1^{B_t} : \mathbf{b}_t^L : \dot{\boldsymbol{\eta}}^L - \mathbf{b}_t^L : \dot{\boldsymbol{\eta}}^L \rangle \quad (9)$$

with $\mathbf{M}_t = \mathbf{B}_t^{-1}$.

Substituting the strain rate equation (6) in the local constitutive law gives the stress rate in each laminate “L”:

$$\dot{\boldsymbol{\sigma}}^L = \mathbf{c}^L : (\dot{\boldsymbol{\varepsilon}}^L - \dot{\boldsymbol{\varepsilon}}^{vpL}) \quad (10)$$

The macroscopic effective behavior is given by: $\dot{\mathbf{E}} = \mathbf{S} : \dot{\boldsymbol{\Sigma}} + \dot{\mathbf{E}}^{vp}$ with $\mathbf{S} = \mathbf{C}^{-1}$, where the effective viscoplastic strain rate $\dot{\mathbf{E}}^{vp}$ calculated at the macroscale is obtained from the stress rate macrohomogeneity condition $\langle \dot{\boldsymbol{\sigma}} \rangle = \dot{\boldsymbol{\Sigma}}$. It yields:

$$\begin{aligned} \dot{\mathbf{E}}^{vp} = & \mathbf{Z} : \langle \mathbf{c}^L : \dot{\boldsymbol{\varepsilon}}^{vpL} \rangle - \mathbf{Z} : \langle \mathbf{c}^L : \mathbf{A}^C : \Gamma_1^{B_t} : (\mathbf{b}_t^L : \dot{\boldsymbol{\eta}}^L - \mathbf{B}_t : \dot{\mathbf{N}}) \rangle \\ & - \mathbf{Z} : \langle \mathbf{c}^L : \mathbf{A}^C : \Gamma_1^C : (\delta \mathbf{c}^L : \dot{\boldsymbol{\varepsilon}}^{vpL} + \mathbf{c}^L : \mathbf{A}^C : \langle \dot{\boldsymbol{\varepsilon}}^{vp} \rangle) \rangle \\ & + \mathbf{Z} : \langle \mathbf{c}^L : \mathbf{A}^C : \Gamma_1^{B_t} : (\delta \mathbf{b}_t^L : \dot{\boldsymbol{\varepsilon}}^{vpL} - \mathbf{b}_t^L : \mathbf{A}^{B_t} : (\mathbf{M}_t : \boldsymbol{\Sigma} + \dot{\mathbf{N}} - \langle \dot{\boldsymbol{\varepsilon}}^{vp} \rangle)) \rangle \\ & - \mathbf{Z} : \langle \mathbf{c}^L : \mathbf{A}^C : (\Gamma_1^C : \mathbf{C} - \Gamma_1^{B_t} : \mathbf{B}_t) : (\dot{\boldsymbol{\varepsilon}}^{vpL} - \mathbf{A}^{B_t} : \langle \dot{\boldsymbol{\varepsilon}}^{vp} \rangle) \rangle \\ & + \mathbf{Z} : \langle \mathbf{c}^L : \mathbf{A}^C : (\Gamma_1^C : \mathbf{C} - \Gamma_1^{B_t} : \mathbf{B}_t) : (\mathbf{A}^{B_t} : \Gamma_1^{B_t} : (\mathbf{b}_t^L : \dot{\boldsymbol{\eta}}^L - \mathbf{B}_t : \dot{\mathbf{N}})) \rangle \end{aligned} \quad (11)$$

with $\mathbf{Z} = (\mathbf{I} - \mathbf{S} : \langle \mathbf{c}^L : \mathbf{A}^C : \Gamma_1^C : \mathbf{c}^L : \mathbf{A}^C \rangle)^{-1} : \mathbf{S}$

At the level of LS (mesoscale), we have $\dot{\boldsymbol{\varepsilon}}^L = \mathbf{s}^L : \dot{\boldsymbol{\sigma}}^L + \dot{\boldsymbol{\varepsilon}}^{vpL}$ with $\dot{\boldsymbol{\varepsilon}}^{vpL} = \mathbf{m}_t^L : \boldsymbol{\sigma}^L + \dot{\boldsymbol{\eta}}^L$. The rank 4 tensors \mathbf{s}^L (resp. \mathbf{c}^L), \mathbf{m}_t^L (resp. \mathbf{b}_t^L), and the rank 2 tensor $\dot{\boldsymbol{\eta}}^L$ are homogenized elastic compliances (resp. moduli), viscoplastic tangent compliances (resp. moduli) and viscoplastic back-extrapolated term for each LS. These tensors are now determined from the homogenization procedure at the mesoscale (see further equations (18), (20), (26), (30), (31)).

3.3. Micro- to mesoscale transition: two-phase LS model

At the mesoscale, we consider an infinite two-phase LS model (see Figure 5). Both phases are ferrite (denoted “ α ”) and austenite (denoted “ γ ”) with volume fractions f^α and f^γ . For the present application, $f^\alpha = 0.25$, therefore $f^\gamma = 1 - f^\alpha = 0.75$. The volume averages of strain and stress tensors over each LS are given by the homogeneity conditions at the mesoscale:

$$\boldsymbol{\varepsilon}^L = \langle \boldsymbol{\varepsilon} \rangle^L = f^\gamma \boldsymbol{\varepsilon}^\gamma + f^\alpha \boldsymbol{\varepsilon}^\alpha \quad (12a)$$

$$\boldsymbol{\sigma}^L = \langle \boldsymbol{\sigma} \rangle^L = f^\gamma \boldsymbol{\sigma}^\gamma + f^\alpha \boldsymbol{\sigma}^\alpha \quad (12b)$$

where $\boldsymbol{\varepsilon}^i = \boldsymbol{\varepsilon}^{e i} + \boldsymbol{\varepsilon}^{vp i} = \mathbf{s}^i : \boldsymbol{\sigma}^i + \boldsymbol{\varepsilon}^{vp i}$ with $i = \alpha, \gamma$. The tensors \mathbf{s}^i , $\boldsymbol{\varepsilon}^i$, $\boldsymbol{\sigma}^i$ and $\boldsymbol{\varepsilon}^{vp i}$ represent the elastic compliances, the strains, the Cauchy stresses and the viscoplastic strains of both phases at the microscale. Under the assumption of mean viscoplastic strain field in each phase, following strain compatibility and balance of linear momentum in the absence of body force, the strains and stresses are therefore piecewise uniform in the two-phase LS model (see e.g. El Omri et al., 2000; Stupkiewicz and Petryk 2002; Franciosi and Berbenni, 2007, 2008; Berbenni et al. 2013; Richeton and Berbenni, 2013; Tiba et al., 2015; Franciosi, 2020; Richeton 2022).

The relationships between the strains and the stresses in each phase α and γ (microscale): $\boldsymbol{\varepsilon}^{\alpha, \gamma}$, $\boldsymbol{\sigma}^{\alpha, \gamma}$ and the strains and stresses at the level of the LS (mesoscale): $\boldsymbol{\varepsilon}^L$, $\boldsymbol{\sigma}^L$ are first calculated in the frame associated with the planar interface, i.e., the HP. Its unit outward normal \mathbf{n} is supposed to be parallel to the \mathbf{e}_2 direction of a Cartesian frame $(\mathbf{e}_1, \mathbf{e}_2, \mathbf{e}_3)$ and is directed from γ to α (see the mesoscale model in Figure 5).

For the 24 KS-OR, the crystallographic planes and directions of the HP are defined in the ferrite frame. Then, the stress and strain tensors calculated in the HP frame are successively rotated in the ferrite frame and in the global frame. The rotation matrix used for the transformation from the HP frame to the ferrite frame is given by the transformations of the HP plane normal vector $[h \ k \ l]$ and in-plane direction vector $[u \ v \ w]$ (see Table 2) into the unit vectors \mathbf{e}_2 and \mathbf{e}_3 , respectively (see Figure 5). The rotation matrix from the ferrite frame to global frame is defined by the three Euler-Bunge angles of the primary ferritic grain (see Table A.2).

In the HP frame, we adopt the following tensor to matrix convention (Nye, 1957) also known as the Voigt's notation, in which pairs of subscripts (ij) and (kl) are converted to single subscripts: $(11)=1$, $(22)=2$, $(33)=3$, (23) and $(32)=4$, (13) and $(31)=5$, (12) and $(21)=6$. In this notation, we will use indices i ranging from 1 to 6. The conventions for strains are the following: $\varepsilon_4 = 2\varepsilon_{23}$, $\varepsilon_5 = 2\varepsilon_{31}$, $\varepsilon_6 = 2\varepsilon_{12}$ and the components of the compliance matrix s_{ij} contain a multiplying factor of 2 if either i or j is equal to 4,5 or 6 and the other index is equal to 1, 2, 3, and, a multiplying factor of 4 if both i and j are equal to 4,5 or 6. Thus, each of the tensor components is associated with a matrix or a vector component.

To determine the strain and stress concentration equations for the mesoscale model, the continuity conditions for stress and strain at the interface are invoked due to traction vector continuity and tangential strain continuity for perfectly bonded interface:

$$\boldsymbol{\varepsilon}_p^\alpha = \boldsymbol{\varepsilon}_p^\gamma = \boldsymbol{\varepsilon}_p^L \quad (13a)$$

$$\boldsymbol{\sigma}_A^\alpha = \boldsymbol{\sigma}_A^\gamma = \boldsymbol{\sigma}_A^L \quad (13b)$$

where the in-plane components of strain and stress tensors are denoted P = 1, 3, 5, and the anti-plane ones are denoted A = 2,4,6, with the following constitutive laws using index notations:

$$\varepsilon_i^{\alpha,\gamma} = s_{ij}^{\alpha,\gamma} \varepsilon_j^{\alpha,\gamma} + \varepsilon_i^{\text{vp}\alpha,\gamma} \quad (i, j = 1,6) \quad (14a)$$

$$\sigma_i^{\alpha,\gamma} = c_{ij}^{\alpha,\gamma} \left(\varepsilon_j^{\alpha,\gamma} - \varepsilon_j^{\text{vp}\alpha,\gamma} \right) = c_{ij}^{\alpha,\gamma} \varepsilon_j^{\alpha,\gamma} - \sigma_i^{\text{vp}\alpha,\gamma} \quad \text{with} \quad \sigma_i^{\text{vp}\alpha,\gamma} = c_{ij}^{\alpha,\gamma} \varepsilon_j^{\text{vp}\alpha,\gamma} \quad (i, j = 1,6) \quad (14b)$$

Starting from equations (14) and using equation (12a) together with equations (13), the strain concentration laws for both phases are obtained:

$$\varepsilon_i^\alpha = \varepsilon_i^L - f^\gamma F_{ik}^c \left(\llbracket c_{kj} \rrbracket \varepsilon_j^L - \llbracket \sigma_k^{\text{vp}} \rrbracket \right) \quad (i, j, k = 1,6; \text{ sum on } j, k) \quad (15a)$$

$$\varepsilon_i^\gamma = \varepsilon_i^L + f^\alpha F_{ik}^c \left(\llbracket c_{kj} \rrbracket \varepsilon_j^L - \llbracket \sigma_k^{\text{vp}} \rrbracket \right) \quad (i, j, k = 1,6; \text{ sum on } j, k) \quad (15b)$$

where $\llbracket \cdot \rrbracket = (\cdot)^\alpha - (\cdot)^\gamma$ denotes the jump of fields or property, and, where the non-zero components of the symmetric matrix F_{ij}^c associated with c_{ij} are given in Appendix B, see equation (B.1).

Conversely, starting from equations (14) and using equation (12b) together with equations (13), the stress concentration laws for both phases are given by (see e.g., Richeton and Berbenni, 2013; Tiba et al., 2015):

$$\sigma_i^\alpha = \sigma_i^L - f^\gamma G_{ik}^s \left(\llbracket s_{kj} \rrbracket \sigma_j^L + \llbracket \varepsilon_k^{\text{vp}} \rrbracket \right) \quad (i, j, k = 1,6; \text{ sum on } j, k) \quad (16a)$$

$$\sigma_i^\gamma = \sigma_i^L + f^\alpha G_{ik}^s \left(\llbracket s_{kj} \rrbracket \sigma_j^L + \llbracket \varepsilon_k^{\text{vp}} \rrbracket \right) \quad (i, j, k = 1,6; \text{ sum on } j, k) \quad (16b)$$

where the non-zero components of the symmetric matrix G_{ij}^s associated with s_{ij} are given in Appendix B, see equation (B.2).

Equations (15) and (16) represent the strain and stress transfers between meso- and micro- scales. Now, let us determine the effective elastic compliance s^L (resp. modulus c^L) of each LS such that $\varepsilon_i^L = s_{ij}^L \sigma_j^L$ or $\sigma_i^L = c_{ij}^L \varepsilon_j^L$. Using equation (12a) together with the linear elastic Hooke's law, we obtain:

$$\varepsilon_i^L = f^\gamma s_{ij}^\gamma \sigma_j^\gamma + f^\alpha s_{ij}^\alpha \sigma_j^\alpha = s_{ij}^L \sigma_j^L \quad (17)$$

Then using both equations (16) with $\varepsilon_k^{\text{vp}} = 0$, together with equation (17), the homogenized elastic compliance for "L" reads (see e.g., Franciosi, 2020; Richeton, 2022):

$$s_{ij}^L = \langle s_{ij} \rangle^L - f^\alpha f^\gamma \llbracket s_{ik} \rrbracket G_{kl}^s \llbracket s_{lj} \rrbracket \quad (18)$$

$$\text{with } \langle s_{ij} \rangle^L = f^\gamma s_{ij}^\gamma + f^\alpha s_{ij}^\alpha.$$

Using equation (12b) together with the linear elastic Hooke's law, we obtain:

$$\sigma_i^L = f^\gamma c_{ij}^\gamma \varepsilon_j^\gamma + f^\alpha c_{ij}^\alpha \varepsilon_j^\alpha = c_{ij}^L \varepsilon_j^L \quad (19)$$

Then, using both equations (15) with $\sigma_k^{vp} = 0$, together with equation (19), the homogenized elastic stiffness for "L" reads:

$$c_{ij}^L = \langle c_{ij} \rangle^L - f^\alpha f^\gamma \llbracket c_{ik} \rrbracket F_{kl}^c \llbracket c_{lj} \rrbracket \quad (20)$$

$$\text{with } \langle c_{ij} \rangle^L = f^\gamma c_{ij}^\gamma + f^\alpha c_{ij}^\alpha.$$

For purely affine viscoplastic two-phase LS, we consider the following thermo-elastic like linear comparison material for both phases α and γ :

$$\dot{\varepsilon}_i^{\alpha,\gamma} = \dot{\varepsilon}_i^{vp\alpha,\gamma} = m_{tij}^{\alpha,\gamma} \sigma_j^{\alpha,\gamma} + \dot{\eta}_i^{\alpha,\gamma} \quad (i, j = 1,6) \quad (21a)$$

$$\sigma_i^{\alpha,\gamma} = b_{tij}^{\alpha,\gamma} \left(\dot{\varepsilon}_j^{\alpha,\gamma} - \dot{\eta}_j^{\alpha,\gamma} \right) = b_{tij}^{\alpha,\gamma} \dot{\varepsilon}_j^{\alpha,\gamma} - b_{tij}^{\alpha,\gamma} \dot{\eta}_j^{\alpha,\gamma} \quad (i, j = 1,6) \quad (21b)$$

with the following continuity conditions for the purely viscoplastic problem:

$$\dot{\varepsilon}_p^\alpha = \dot{\varepsilon}_p^\gamma = \dot{\varepsilon}_p^L \quad (22a)$$

$$\sigma_A^\alpha = \sigma_A^\gamma = \sigma_A^L \quad (22b)$$

and the volume averages on the laminate:

$$\dot{\varepsilon}_i^L = \langle \dot{\varepsilon}_i \rangle^L = f^\gamma \dot{\varepsilon}_i^\gamma + f^\alpha \dot{\varepsilon}_i^\alpha \quad (23a)$$

$$\sigma_i^L = \langle \sigma_i \rangle^L = f^\gamma \sigma_i^\gamma + f^\alpha \sigma_i^\alpha \quad (23b)$$

For this purely viscoplastic problem, similar strain concentration equations are found by substituting in equation (15) $\dot{\varepsilon}_i^\alpha, \dot{\varepsilon}_i^\gamma, \dot{\varepsilon}_j^L, F_{ik}^{bt}, b_{tkj}, b_{tkj} \dot{\eta}_j$ for $\varepsilon_i^\alpha, \varepsilon_i^\gamma, \varepsilon_j^L, F_{ik}^c, c_{kj}, \sigma_k^{vp}$, respectively:

$$\dot{\varepsilon}_i^\alpha = \dot{\varepsilon}_i^L - f^\gamma F_{ik}^{bt} \left(\llbracket b_{tkj} \rrbracket \dot{\varepsilon}_j^L - \llbracket b_{tkj} \dot{\eta}_j \rrbracket \right) \quad (i, j, k = 1,6; \text{ sum on } j, k) \quad (24a)$$

$$\dot{\varepsilon}_i^\gamma = \dot{\varepsilon}_i^L + f^\alpha F_{ik}^{bt} \left(\llbracket b_{tkj} \rrbracket \dot{\varepsilon}_j^L - \llbracket b_{tkj} \dot{\eta}_j \rrbracket \right) \quad (i, j, k = 1,6; \text{ sum on } j, k) \quad (24b)$$

where the non-zero components of the symmetric matrix F_{ij}^{bt} associated with b_{tij} are given by substituting b_{tij} for c_{ij} in equation (B.1). Using equation (21b) together with equation (23b) yields:

$$\sigma_i^L = f^\gamma (b_{tij}^Y \dot{\epsilon}_j^Y - b_{tij}^Y \dot{\eta}_j^Y) + f^\alpha (b_{tij}^\alpha \dot{\epsilon}_j^\alpha - b_{tij}^\alpha \dot{\eta}_j^\alpha) = b_{tij}^L \dot{\epsilon}_j^L + \zeta_i^L \quad (25)$$

with the back-extrapolated stress $\zeta_i^L = -b_{tij}^L \dot{\eta}_j^L$. Introducing both equations (24) in equation (25) yields:

$$b_{tij}^L = \langle b_{tij} \rangle^L - f^\alpha f^\gamma [[b_{tik}]] F_{kl}^{bt} [[b_{tlj}]] \quad (26)$$

$$\zeta_i^L = \langle \zeta_i \rangle^L + f^\alpha f^\gamma [[b_{tik}]] F_{kl}^{bt} [[\zeta_j]] \quad (27)$$

with $\langle b_{tij} \rangle^L = f^\gamma b_{tij}^Y + f^\alpha b_{tij}^\alpha$ and $\langle \zeta_i \rangle^L = f^\gamma \zeta_i^Y + f^\alpha \zeta_i^\alpha$.

Conversely, similar stress concentration equations are found by substituting in equation (16): G_{ik}^{mt} , m_{tkj} , $\dot{\eta}_k$ for G_{ik}^s , s_{kj} , ϵ_k^{vp} , respectively:

$$\sigma_i^\alpha = \sigma_i^L - f^\gamma G_{ik}^{mt} \left([[m_{tkj}]] \sigma_j^L + [[\dot{\eta}_k]] \right) \quad (i, j, k = 1, 6; \text{sum on } j, k) \quad (28a)$$

$$\sigma_i^Y = \sigma_i^L + f^\alpha G_{ik}^{mt} \left([[m_{tkj}]] \sigma_j^L + [[\dot{\eta}_k]] \right) \quad (i, j, k = 1, 6; \text{sum on } j, k) \quad (28b)$$

where the non-zero components of the symmetric matrix G_{ij}^{mt} associated with m_{tij} are given by substituting m_{tij} for s_{ij} in equation (B.2). Using equation (21a) together with equation (23a) yields

$$\dot{\epsilon}_i^L = f^\gamma (m_{tij}^Y \sigma_j^Y + \dot{\eta}_i^Y) + f^\alpha (m_{tij}^\alpha \sigma_j^\alpha + \dot{\eta}_i^\alpha) = m_{tij}^L \sigma_j^L + \dot{\eta}_i^L \quad (29)$$

Then, using equations (28) in equation (29) yields:

$$m_{tij}^L = \langle m_{tij} \rangle^L - f^\alpha f^\gamma [[m_{tik}]] G_{kl}^{mt} [[m_{tlj}]] \quad (30)$$

$$\dot{\eta}_i^L = \langle \dot{\eta}_i \rangle^L - f^\alpha f^\gamma [[m_{tik}]] G_{kl}^{mt} [[\dot{\eta}_l]] \quad (31)$$

with $\langle m_{tij} \rangle^L = f^\gamma m_{tij}^Y + f^\alpha m_{tij}^\alpha$ and $\langle \dot{\eta}_i \rangle^L = f^\gamma \dot{\eta}_i^Y + f^\alpha \dot{\eta}_i^\alpha$.

It is noteworthy that equations (18) and (20) and equations (26) and (30) are consistent from the homogenization theory since $\mathbf{s}^L = \mathbf{c}^{L-1}$, $\mathbf{m}_t^L = \mathbf{b}_t^{L-1}$ (see e.g. Qu and Cherkaoui, 2006). Furthermore, it can be seen from these expressions that the method is not restricted to iso-stress (Reuss) or iso-strain (Voigt) assumptions. These ones are used to model duplex steels in the literature. For instance, Verhaeghe et al. (1996) and M'Cirdi (2000) used a Taylor (1938)'s model, which is

equivalent to iso-strain assumption. In section 4, we will show that some HP configurations do not lead to iso-strain states.

3.4. Microscale: single crystal's behavior

The elasto-viscoplastic behavior is described in each phase α and γ at the microscale within a crystal plasticity framework. The constitutive equations developed by Méric and Cailletaud (1991a,b) are used to model the behavior of crystalline laths in both the f.c.c. structure for austenitic laths and in the b.c.c. structure for ferritic laths. This model depends on a limited number of materials parameters. The viscoplastic strain rate is given by crystal plasticity in both phases:

$$\dot{\boldsymbol{\epsilon}}^{vp} = \sum_{s=1}^N \mathbf{R}^s \dot{\gamma}^s \quad (32)$$

Equation (32) describes the sum of the contributions of all active slip systems (i.e. $\dot{\gamma}^s \neq 0$) in each single crystalline phase. The driving force for slip is given by the resolved shear stress τ^s , defined as:

$$\tau^s = \mathbf{R}^s : \boldsymbol{\sigma} \quad (33)$$

with \mathbf{R}^s the symmetric Schmid orientation tensor:

$$R_{ij}^s = \frac{1}{2} (n_i^s l_j^s + n_j^s l_i^s) \quad (34)$$

where n_i^s and l_i^s are unit vectors normal to slip plane and parallel to slip directions.

The behavior of the single crystal (cubic crystals for both phases) is supposed to be elastic-viscoplastic for both phases at small strains, where plastic distortion results from crystallographic slips on specific systems s defined by a plane normal \mathbf{n}^s and a slip direction \mathbf{l}^s . Here, the effect of lattice rotation evolution is neglected as in previous studies on the same material (see Bugat et al., 1999; Bugat, 2000). For f.c.c. crystals (austenite), 12 octahedral slip systems of type (111) $\langle 110 \rangle$. Following previous studies in duplex steels (Bugat et al., 1999; Bugat 2000; Verhaeghe et al. 1996, 1997), we assume that only the dense systems (110) $\langle 111 \rangle$ are activated in the ferrite (b.c.c). This assumption is made due to the KS-OR, which favors such family of slip systems in the b.c.c. structure.

The phenomenological model with hardening variables developed by Méric and Cailletaud (1991a,b) is used to describe the viscoplastic slip rate $\dot{\gamma}^s$:

$$\dot{\gamma}^s = \left\langle \frac{|\tau^s - x^s| - r^s}{K} \right\rangle^n \text{sign}(\tau^s - x^s) \quad (35)$$

where the Macaulay brackets $\langle . \rangle$ describe the ramp function in equation (35). In this equation, x^s and r^s are the kinematic and the isotropic hardening shear stresses, respectively, given by their rates:

$$\dot{x}^s = c\dot{\gamma}^s - dx^s|\dot{\gamma}^s| \quad (36)$$

and:

$$\dot{r}^s = \sum_{r=1}^N bqH_{sr} \exp(-bv^r)|\dot{\gamma}^r| \quad (37)$$

where $v^r = \int |\dot{\gamma}^r| dt$.

In the above equations, K and n are two material coefficients characterizing the viscous effect, c , b , d and q are hardening parameters, H_{sr} is an $N \times N$ matrix describing the interactions between the different slip systems, where N is the total number of the slip systems in both austenite and ferrite single crystals (here $N = 12$ for both the f.c.c. and b.c.c. slip systems, see Appendix C). Therefore, at the grain level, the viscoplastic strain rate tensor is given by:

$$\dot{\boldsymbol{\epsilon}}^{vp} = \sum_{s=1}^N \mathbf{R}^s \left\langle \frac{|\tau^s - x^s| - r^s}{K} \right\rangle^n \text{sign}(\tau^s - x^s) \quad (38)$$

According to the ‘‘affine’’ formulation used in this study (equation (2)), the tangent viscoplastic compliance tensor $\mathbf{m}_t = \partial \dot{\boldsymbol{\epsilon}}^{vp} / \partial \boldsymbol{\sigma}$ and the back-extrapolated viscoplastic strain rate tensor $\dot{\boldsymbol{\eta}}$ write in index notation, as:

$$m_{tijkl} = \sum_{s=1}^N \frac{n}{K} \left\langle \frac{|\tau^s - x^s| - r^s}{K} \right\rangle^{n-1} R_{ij}^s R_{kl}^s \quad (39)$$

and:

$$\dot{\eta}_{ij} = \sum_{s=1}^N R_{ij}^s \left\langle \frac{|\tau^s - x^s| - r^s}{K} \right\rangle^n \text{sign}(\tau^s - x^s) - \sum_{s=1}^N \frac{n}{K} \left\langle \frac{|\tau^s - x^s| - r^s}{K} \right\rangle^{n-1} R_{ij}^s \tau^s \quad (40)$$

using equation (33). Then, equations (39) and (40) are used in equations (30) and (31).

4. Simulation results

4.1. Model parameters

To determine materials parameters, the tensile response of the CF8M material is predicted with the three-scale homogenization model, where 15 reconstructed primary ferritic grains are considered with volume fractions extracted from EBSD data, and crystallographic orientations given in Table A.2 (Appendix A). These orientations are defined with respect to the global Cartesian frame (X, Y, Z). Each primary ferritic grain is made of 24 laminate structures (LS) (lath clusters) included in spherical domains with equal volume fractions $f^L = 1/24$. It is then assumed that the occurrence probability of each variant is equal with no specific variant selection. This assumption follows the EBSD analysis, which does not display the predominance of specific variants. Therefore, the Representative Volume Element (RVE) used for the three-scale model to identify materials parameters contains 360 spherical grains (15×24) with LS structures (see Figure 5).

First, the elastic properties of the material are supposed to be isotropic with $E = 200$ GPa (Young's modulus) and $\nu = 0.3$ (Poisson ratio). The crystal plasticity hardening parameters (r_0, b, q) were identified on two tensile curves obtained for the non-aged material (Figure 7(a)) and the aged one (Figure 7(b)), and for an applied strain rate of $\dot{\epsilon} = 2 \times 10^{-4} s^{-1}$ in the X-direction (tensile direction). Following the parameter identification performed by Bugat (2000) for similar duplex steels, we considered the same viscosity parameters: $n = 10$, $K = 20$, and we also assumed that $H_{sr} = 1$. Therefore, the identified crystal plasticity parameters are gathered in Table 3 for the non-aged and aged material.

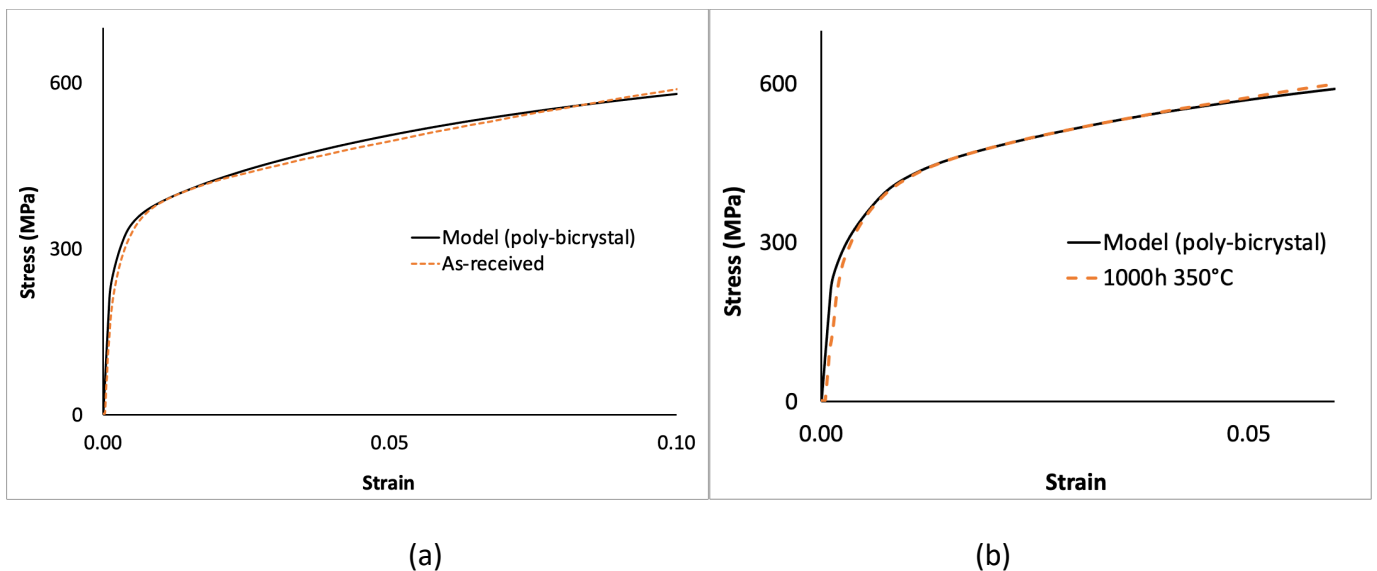


Figure 7. Identification of crystal plasticity parameters for both phases using the tensile curves of the as-received specimen (a); and the aged specimen (b).

Table 3. Viscoplastic flow rule and hardening parameters (Méric-Cailletaud's law) for both phases identified on the non-aged and aged experimental tensile curves.

	n	K (MPa. s ^{1/n})	r_0 (MPa)	b	q (MPa)	c (MPa)	d	H_{sr}
Austenite FCC {111} <110> 12 slip systems	10	20	95	13	36	0	0	1
Non-aged Ferrite BCC {110} <111> 12 slip systems	10	20	260	20	95	0	0	1
Aged Ferrite: BCC {110} <111> 12 slip systems	10	20	400	25	105	0	0	1

4.2. Numerical assessment for one KS-OR variant at mesoscale

Ferrite: 25 %

Austenite: 75 %

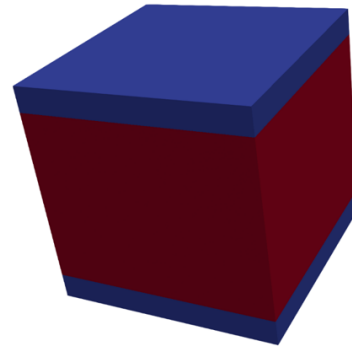
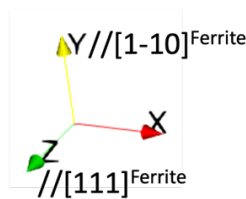


Figure 8. Two-phase laminate configuration for the first KS-OR in the list of Table 2. The calculations are made with the mean field mesoscale model for one laminate structure (LS).

Numerical comparisons with unit cell calculations using the EVPFFT model.

In a first part, it is important to discuss and validate the micromechanical model chosen at the mesoscale in Figure 5. One KS-OR variant is chosen, i.e. the first variant among the list of the 24 variants denoted V1 in Table 2. For these simulations, the Cartesian coordinate system (X, Y, Z) is fixed with the HP (i.e., the interface between both phases) as shown in Figure 8, with unit normal \mathbf{n}

parallel to the Y-axis ($// [1 \bar{1}0]$ in ferrite frame), while the X-axis and the Z-axis ($// [1 1 1]$ in ferrite frame) are parallel to the HP (see Figure 8).

The volume fraction of ferrite (blue colored phase in Figure 8) is set to 25% to be consistent with the experimental data, and the Euler-Bunge angles for ferrite in this configuration is given by: $\phi_1 = 90^\circ, \phi = 54.74^\circ, \phi_2 = 45^\circ$. The volume fraction of austenite (red colored phase on Figure 10) is set to 75% with Euler-Bunge angles: $\phi_1 = 125.27^\circ, \phi = 90^\circ, \phi_2 = 45^\circ$.

The monotonic tensile responses simulated with the mean field model along the X- and Y-directions with applied strain rate $\dot{E} = 10^{-3} s^{-1}$ are first compared to full-field calculations performed with the elasto-viscoplastic fast Fourier transform (EVPFFT) method. Numerical details about this method can be found in Lebensohn et al. (2012), Djaka et al. (2020) and Berbenni et al. (2020). In Figure 9, the average stresses vs. average strains over the LS (black colored curves), ferrite (blue colored curve) and austenite (red colored curve) are reported. Here, the EVPFFT formulation was adapted from the earlier version of Lebensohn et al. (2012) with the numerical implementation of the Méric and Cailletaud (1990a,b)'s crystal plasticity laws reported in section 3.4 (see dotted curves). It is then checked that a very good match is obtained between both methods. However, the present analytical model is more relevant for multiscale computations (see flowchart in Figure 6), because it does not need full field calculations.

In Figure 10, it is shown that the largest stress differences between both phases and between the overall behavior of the laminate composite are obtained for the the X- and Z- tensile loading directions, i.e., parallel to the HP. Then, large incompatibility stresses are observed for these directions, while uniform strain is present. In contrast, due to traction continuity at the HP, the same stress is obtained in both phases for the case where the tensile direction is parallel to the Y-direction, but the strains are not uniform anymore. Therefore, the classic iso-strain assumption frequently used in the literature is not valid anymore in this configuration.

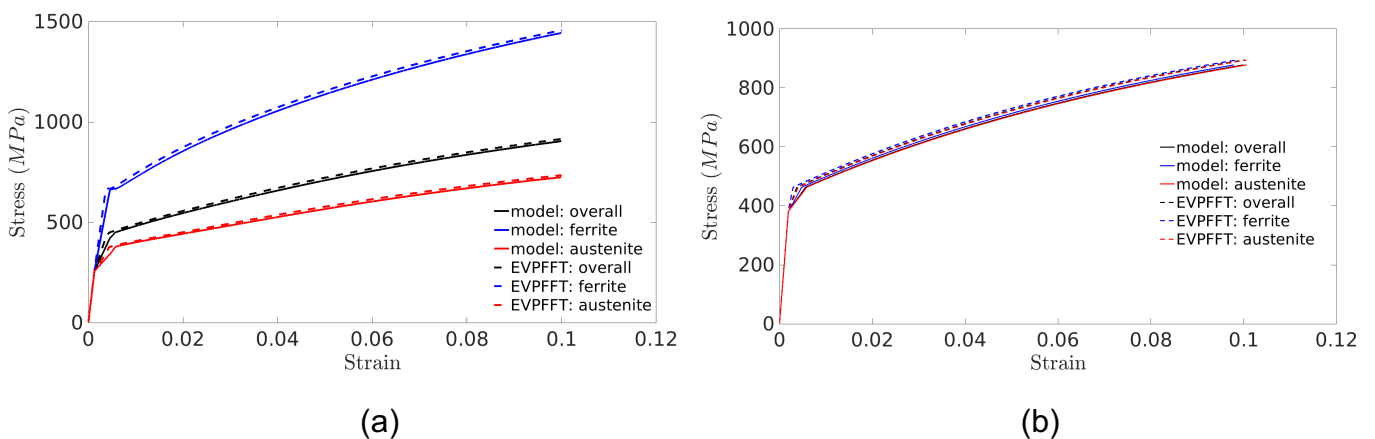


Figure 9. Monotonic tensile responses (true stresses/true strains) simulated with the mean field model at mesoscale (solid lines) along the: (a) X-, (b) Y-, with applied strain rate $\dot{\epsilon} = 10^{-3} s^{-1}$ compared to full-field EVPFFT calculations with periodic boundary conditions and same applied strain rate (dotted lines). The reported stresses are the average stresses in ferrite, austenite and in the LS (overall).

The responses of the LS model are now compared with the individual single crystalline responses, which are simulated separately for same boundary conditions (see the curves with dotted lines in Figure 10). The objective is to study the influence of the strain-hardening behavior of each phase compared to the role of incompatibility stresses on the stress/strain responses and on slip activity. Regarding the X-direction, a larger hardening rate is observed in the case of the LS in both phases (solid lines) compared to single crystalline responses (dotted lines) due to internal stresses in both phases, see Figure 10(a). The active slip systems are B4, C1 for single austenite, and 2A, 4D for single ferrite (see Tables C.1 and C.2 in Appendix C for the conventions used for slip systems), which correspond to a double slip configuration in both crystals and follows the classic Schmid factor analysis. When the LS is considered with the KS OR (V1), slip activity changes from double to multiple slip and additional slip systems are activated: B5, A3, C5, A2, for austenite, and 6A, 6D, 1C, 3C, for ferrite. In the Y-direction, the single crystal hardening curves exhibit a difference of about 500 MPa at 10% of strain, where ferrite (b.c.c.) is harder than austenite (f.c.c.), see Figure 10(b). In contrast, the LS leads to equal stress in both phases, which corresponds to the volume average of the individual single crystalline stresses (composite effect). For single crystals, slip activity is governed by 4 slip systems for ferrite (2A, 3A, 1D, 4D) and 6 ones for austenite (B2, C3, B5, C5, A2, A3). It is noteworthy that the same active slip systems are present in the LS, due to the iso-stress condition in this case. The uniaxial tension in the Z-direction (i.e. // [1 1 1] in ferrite frame) displays similar behavior between single crystal responses and phase responses in the LS, see Figure 10(c). In this case, there is a negligible composite effect, so that the hardening behavior in both phases of the laminate is mainly dictated by the single crystalline behaviors. The slip analysis shows similar trends between single crystalline and bi-crystalline responses with the activations of B2, B4, C1, C3 for austenite and 3C, 1C, 6D, 6A, 1D, 3A for ferrite.

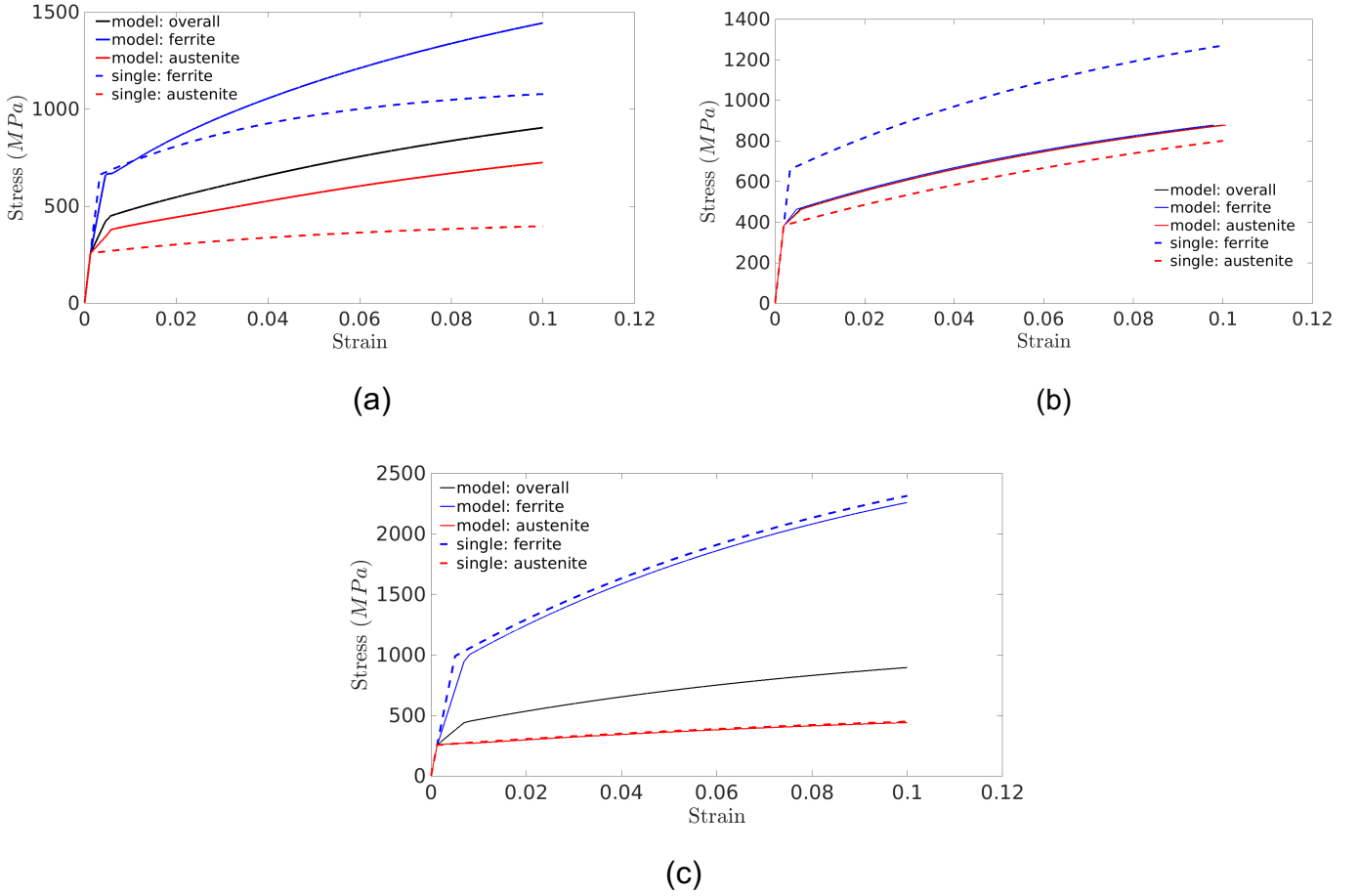


Figure 10. Monotonic tensile responses (true stresses/true strains) simulated with the mean field model at meso-scale (solid lines) along the: (a) X-, (b) Y-, (c) Z-directions with applied strain rate $\dot{E} = 10^{-3} s^{-1}$ compared to single crystalline responses with same boundary conditions (dotted lines). The reported stresses are the average stresses in ferrite, austenite and in the laminate (overall).

4.3. Mechanical behavior of one primary ferritic grain containing 24 KS-OR variants: tensile loading along the [100] direction in ferrite frame

Let us consider a first case where the calculations are performed in the Cartesian frame related to ferrite. Hence, the crystallographic orientation of ferrite is supposed to be given by the Euler-Bunge angles: $\phi_1 = 0^\circ, \phi = 0^\circ, \phi_2 = 0^\circ$. In this case, the Euler-Bunge angles for the 24 KS-OR variants are given in Table 2. The RVE used for the three-scale model contains 24 spherical grains with LS structures (see Figure 5) for one primary ferritic grain. It is subjected to a tensile loading along the X-axis with applied strain rate $\dot{E} = 10^{-3} s^{-1}$.

Figure 11 shows the distribution of stresses along the tensile direction in ferrite (σ_{11}) corresponding to the stresses parallel to the [100] direction in ferrite frame, as a function of applied tensile strain

(E_{11}). These calculations are useful to determine the stresses normal to a cleavage plane, which is of $\{100\}$ -type in ferrite frame (Bugat et al. 1999, 2001; Bugat, 2000, M’Cirdi, 2000; M’Cirdi et al., 2001). Three groups of variants with different mechanical behaviors can be clearly identified: two groups exhibit stresses reaching a range between 500-600 MPa at 10% of tensile strain, and one group reflects higher stresses exceeding 1000 MPa at 10% of tensile strain.

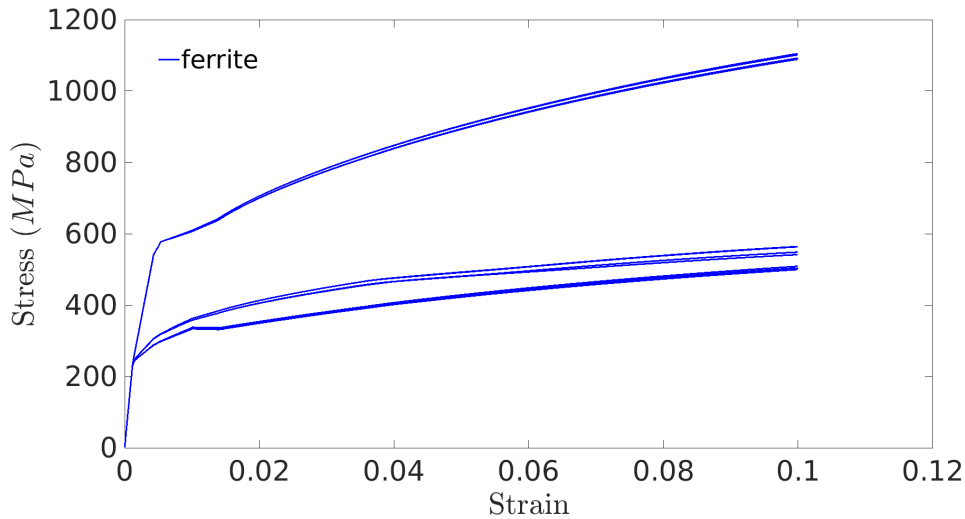
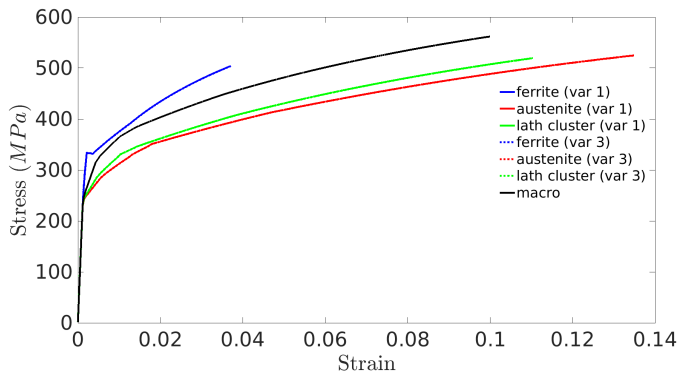
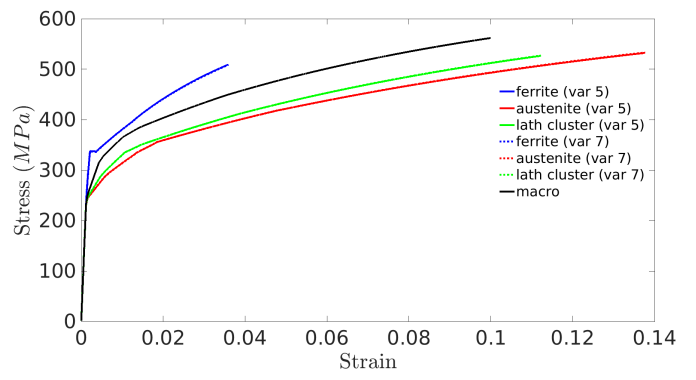


Figure 11. True stresses in ferrite as a function of macroscopic tensile true strain (in the X-direction, i.e., the $[100]$ crystallographic direction in ferrite frame) for the 24 KS-OR variants.

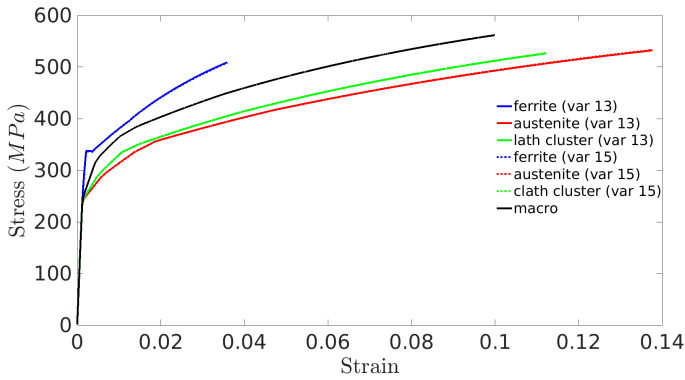
The analysis of these three groups in terms of local strains and stresses in both phases is reported. The first group corresponds to variants V1, V3, V5, V7, V13, V15, V21, V23 with only Bain group B1 (see Figure 12). The second one corresponds to variants V2, V4, V6, V8, V14, V16, V22, V24 (see Figure 13), and the third one corresponds to variants V9, V10, V11, V12, V17, V18, V19, V20 (see Figure 14). We notice that each of the three groups contains specific HP. According to Table 2, it is seen that the first two groups with lower stresses (Figures 12 and 13) contain HP: H1, H2, H3, H4, whereas the third group, which give higher stresses (Figure 14) is only constituted of HP: H5 and H6. Therefore, it is shown that the HP parallel to the loading direction (X-axis) like H5 and H6 give to highest strains and stresses in ferrite associated with these variants. The stresses in ferrite and austenite for these variants are much different from the averaged stress at the mesoscale for each variant (green colored solid lines) and the macroscopic average stress at the scale of the primary ferritic grain (black colored solid lines). The strains in both phases are uniform. This mechanical behavior looks like the single LS responses in Figures 10(a) and 10(c). In the case of HP: H1 to H4, they are oriented at 45° with respect to the X-tensile loading axis. For each variant with H1 to H4, stress difference is not observed but a large strain discrepancy is present between both phases and the mesoscale and macroscopic average responses (see Figures 12 and 13).



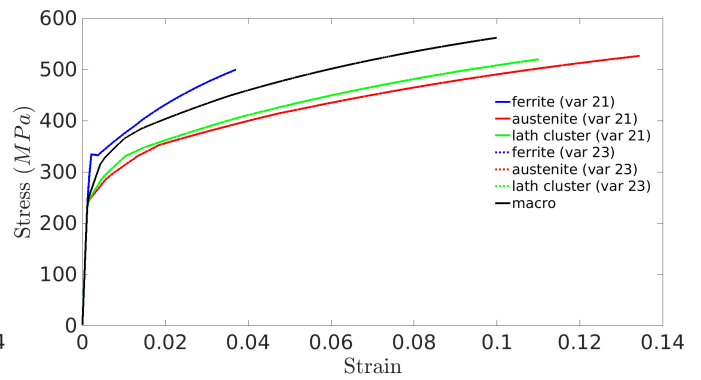
(a)



(b)

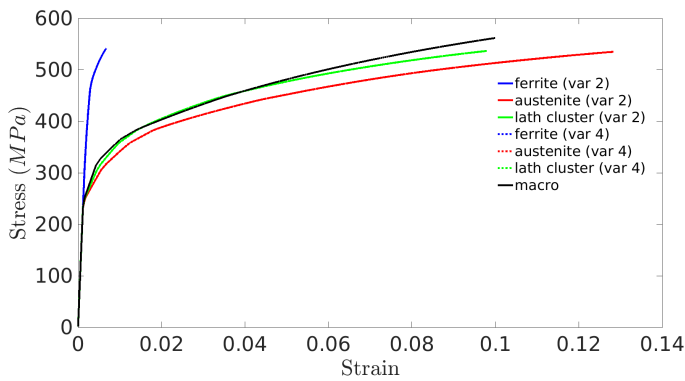


(c)

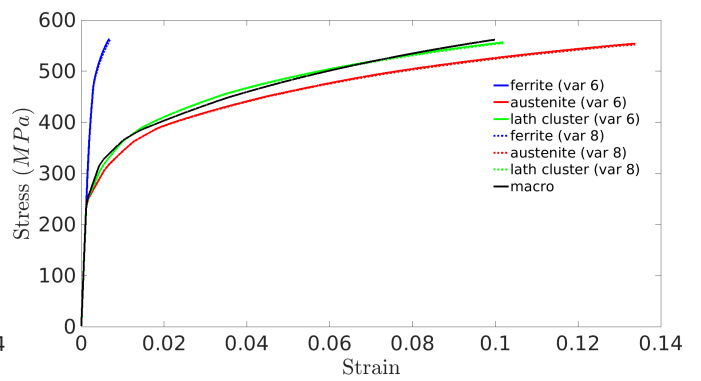


(d)

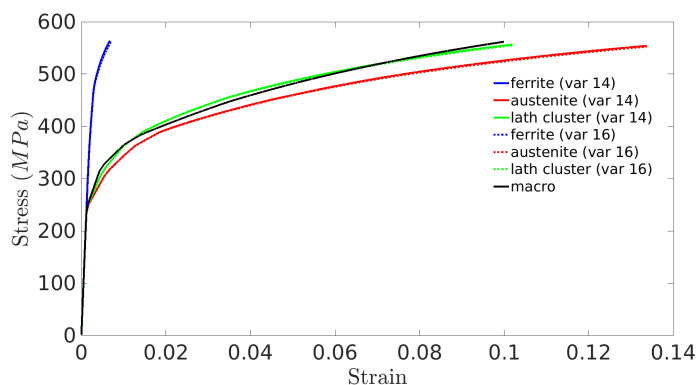
Figure 12. True stress/true strain responses according to the X-direction for the *first group of variants*: (a) 1, 3 (H1, B1); (b) 5, 7 (H3, B1); (c) 13, 15 (H4, B1); (d) 21, 23 (H2, B1)



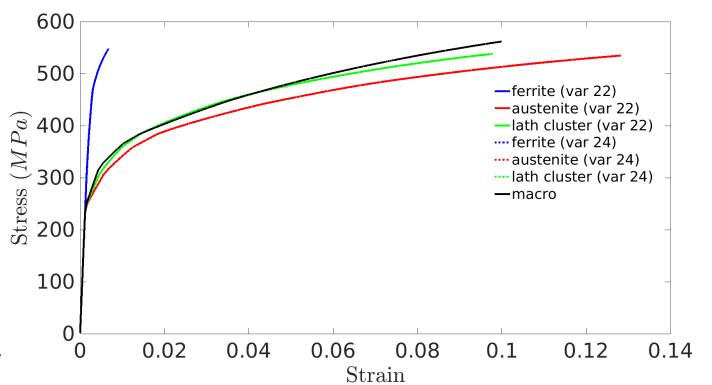
(a)



(b)



(c)



(d)

Figure 13. True stress/true strain responses according to the X-direction for the *second group of variants*: (a) 2, 4 (H2, B2); (b) 6, 8 (H4, B3); (c) 14, 16 (H3, B3); (d) 22, 24 (H1, B2)

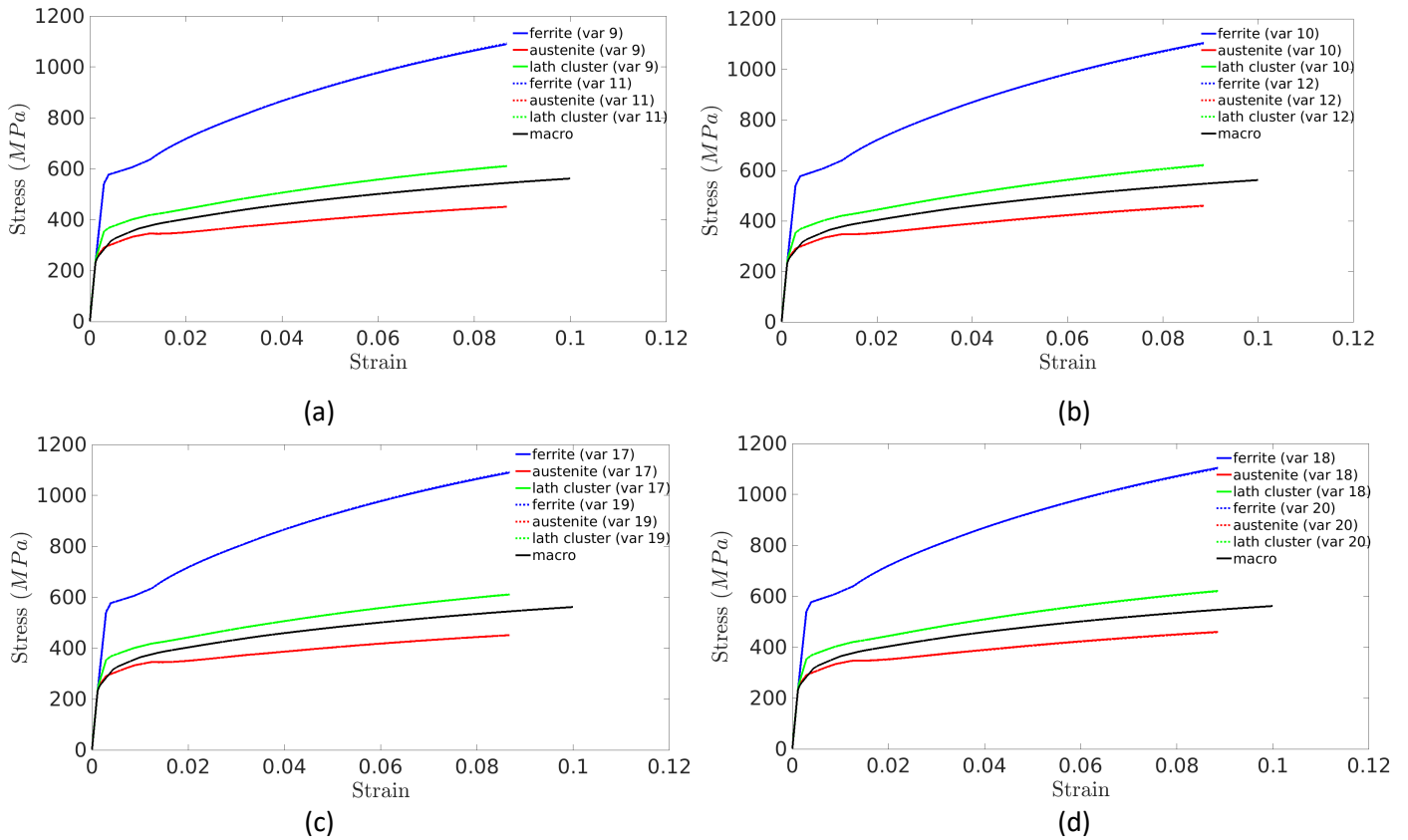


Figure 14. True stress/true strain responses according to x-direction for the *third group of variants*: (a) 9, 11 (H5, B2); (b) 10, 12 (H6, B3); (c) 17, 19 (H6, B2); (d) 18, 20 (H5, B6).

4.4. Effect of the primary ferritic grain crystallographic orientation on the mechanical responses

In this section, the role of primary ferritic grain orientation is investigated. Then, we consider here the crystallographic orientation of the first ferritic grain in the list: $\phi_1 = 18.11^\circ, \phi = 40.12^\circ, \phi_2 = 7.52^\circ$ (see Table A.2 in Appendix A). It corresponds to the largest grain of the specimen (green colored on the left part of Figure 1). Figure 15 shows the stress heterogeneities in ferrite among variants for this orientation (here the stress component along the X-direction). Overall, these stress heterogeneities are more important than for the initial orientation $\phi_1 = 0^\circ, \phi = 0^\circ, \phi_2 = 0^\circ$, see Figure 11. The clear separation into three well defined groups of variants as in Figure 11 vanishes. For each previous group, there is now a large scatter of stress responses in ferrite due to primary ferritic grain orientation which breaks the symmetries of the HP in the KS-OR variants with respect to the loading axis. Figure 16 shows the axial stresses for austenite, ferrite and the averaged

responses at the mesoscale and at the macroscale for the first group (V1, V3, V5, V7, V13, V15, V21, V23). It is shown that the highest stresses in ferrite are found for variants V5, V7, V21, V23. Figure 17 shows the axial stresses for austenite, ferrite and the averaged responses at the mesoscale and at the macroscale for the second group (V2, V4, V6, V8, V14, V16, V22, V24). It is shown that the stresses in ferrite are lower than the ones in the first group: the highest stresses are found with V2, V14, V16. In these groups, the variants V6, V8, V13, V15 still exhibit very low strains in ferrite compared to austenite as in the case of the initial orientation (see Figures 12(b) and 13(b)). In the third group of variants (V9, V10, V11, V12, V17, V18, V19, V20), the stresses in ferrite remain high (around 1000 MPa at 10% of strain) and the strains are more uniform, see Figure 18, which corroborates the results found in Figure 14. However, there are now small discrepancies between the different variants of this group due to the crystallographic orientation of the ferritic grain.

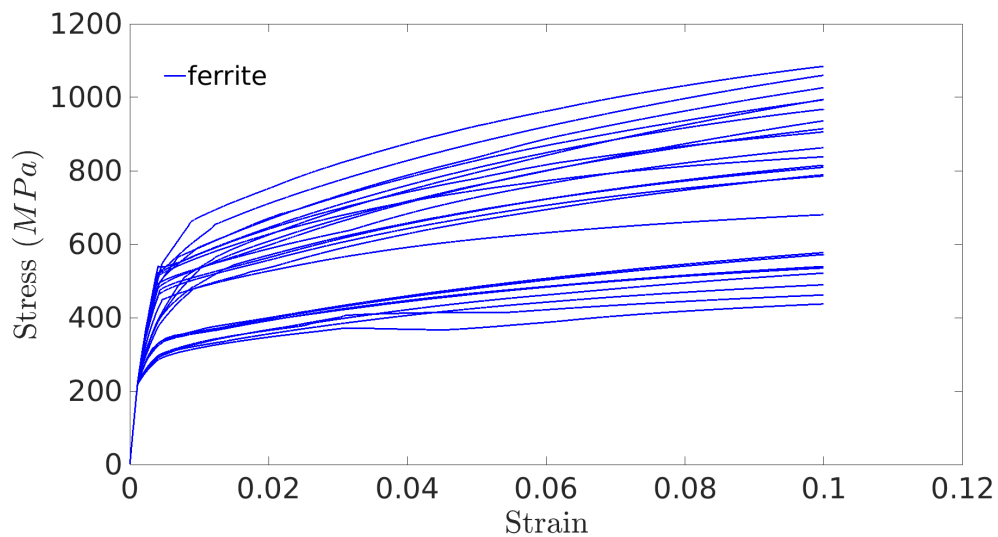
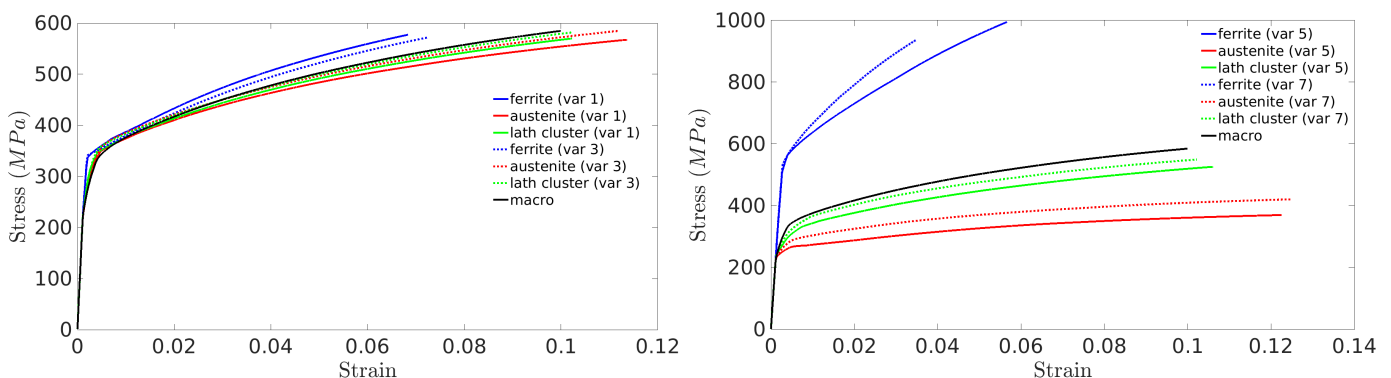


Figure 15. True stresses in ferrite for the 24 different KS-OR variants as a function of macroscopic true strain according to the X-direction for the ferrite orientation: $\phi_1 = 18.11^\circ$, $\phi_2 = 40.12^\circ$, $\phi_3 = 7.52^\circ$.



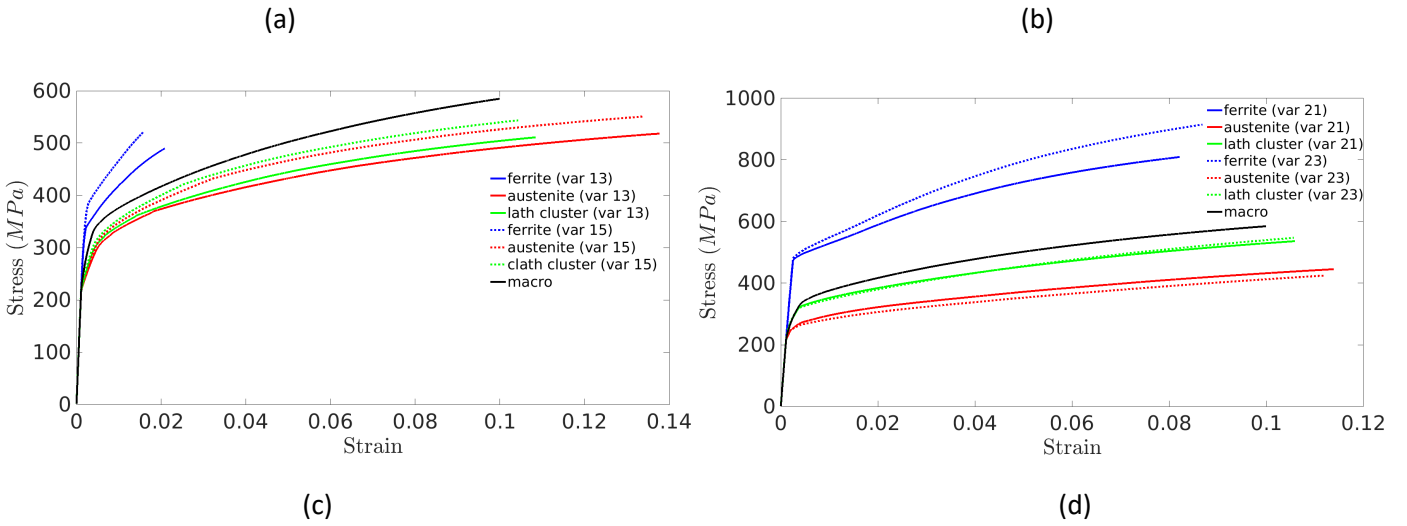


Figure 16. True stress/true strain responses according to the X-direction for the *first group of variants*: (a) 1, 3 (H1, B1); (b) 5, 7 (H3, B1); (c) 13, 15 (H4, B1); (d) 21, 23 (H2, B1)

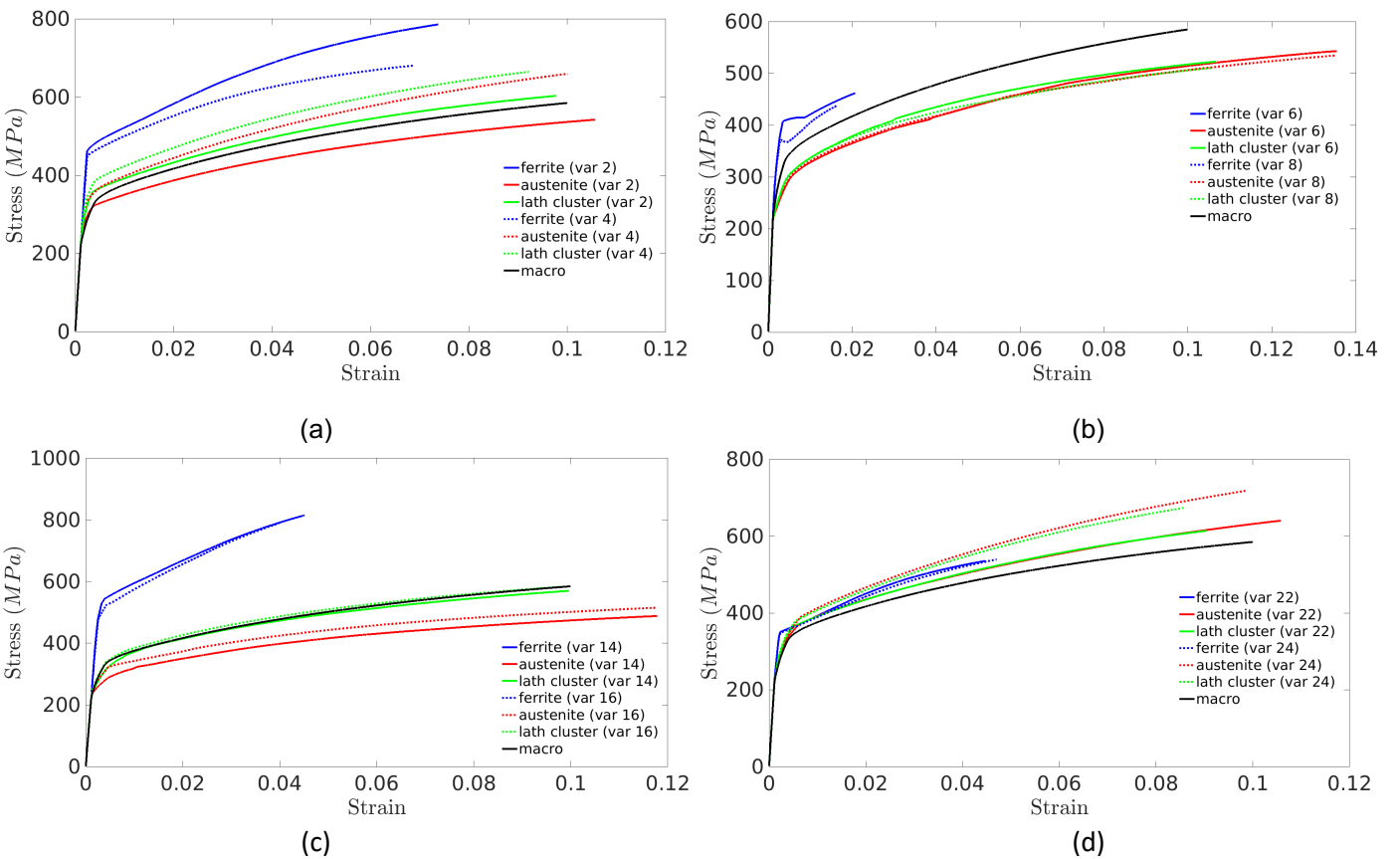


Figure 17. True stress/true strain responses according to X-direction for the *second group of variants*: (a) 2, 4 (H2, B2); (b) 6, 8 (H4, B3); (c) 14, 16 (H3, B3); (d) 22, 24 (H1, B2)

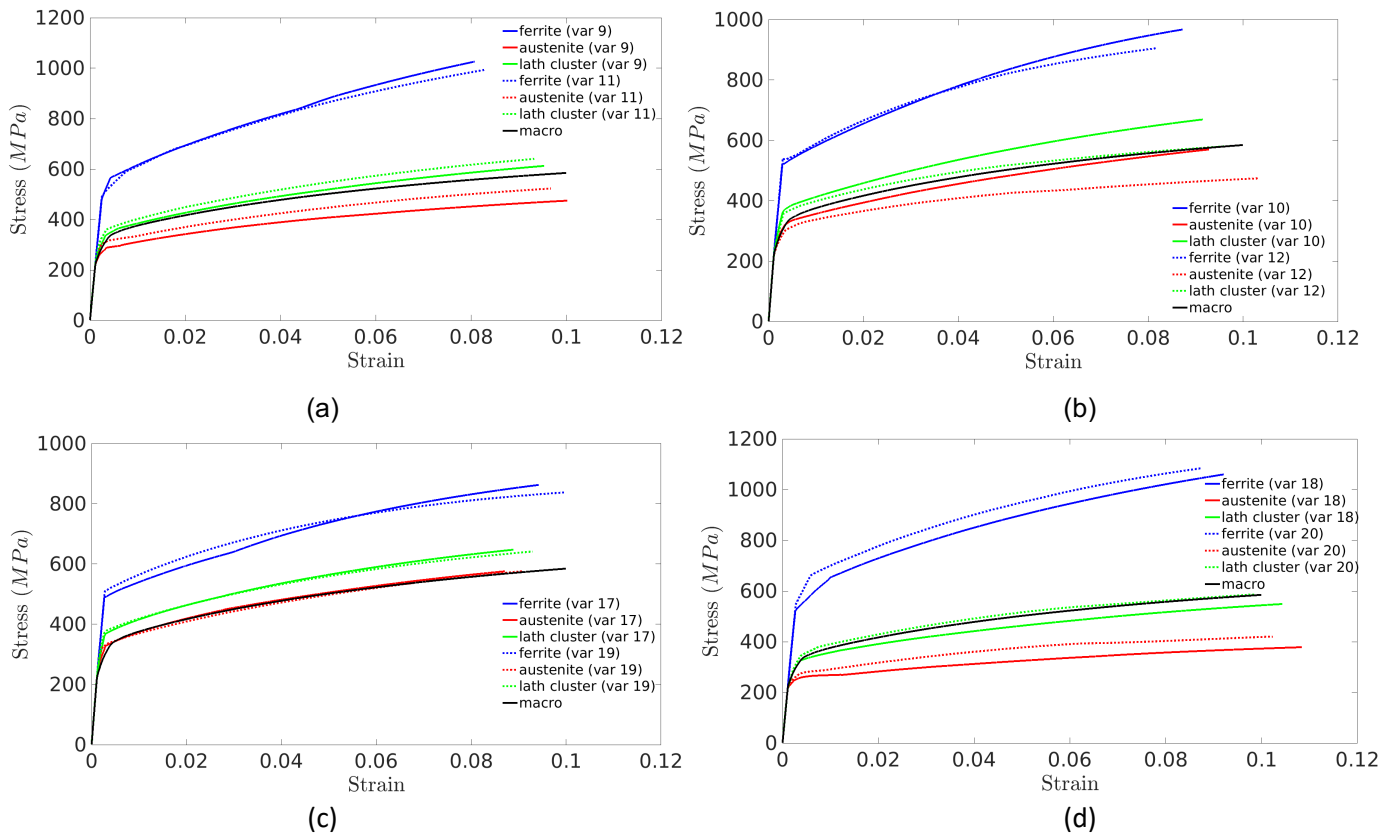


Figure 18. True stress/true strain responses according to X-direction for *the third group of variants*: (a) 9, 11 (H5, B2); (b) 10, 12 (H6, B3); (c) 17, 19 (H6, B2); (d) 18, 20 (H5, B6)

4.5. Simulation of aging effects

Since the microstructure of ferrite evolves during aging, it becomes harder and more brittle, these effects can be simulated by considering different hardening parameters for ferrite only (r_0 and q), while assuming the same materials parameters for austenite. The materials parameters were identified using the tensile curve of the aged specimen until 6% of strain (see Table 3 and Figure 7(b)).

Figure 19 displays the comparisons between stress/strain responses according to the X-direction obtained for the three groups of variants with materials parameters identified for the as-received and the aged specimen. The first group is represented by variants 1, 3 (H1, B1), see Figures 19(a,b). The second group of variants is represented by variants 2, 4 (H2, B2), see Figures 19(c,d). The third group of variants is represented by variants 9, 11 (H5, B2), see Figures 19(e,f). It is seen that aging is at the origin of an increase of the stress in ferrite. Therefore, incompatibility stresses and strains between both phases are more important in the case of the aged specimen. This trend has a consequence in the internal stresses (i.e., backstress) at the different scales (see section 4.7).

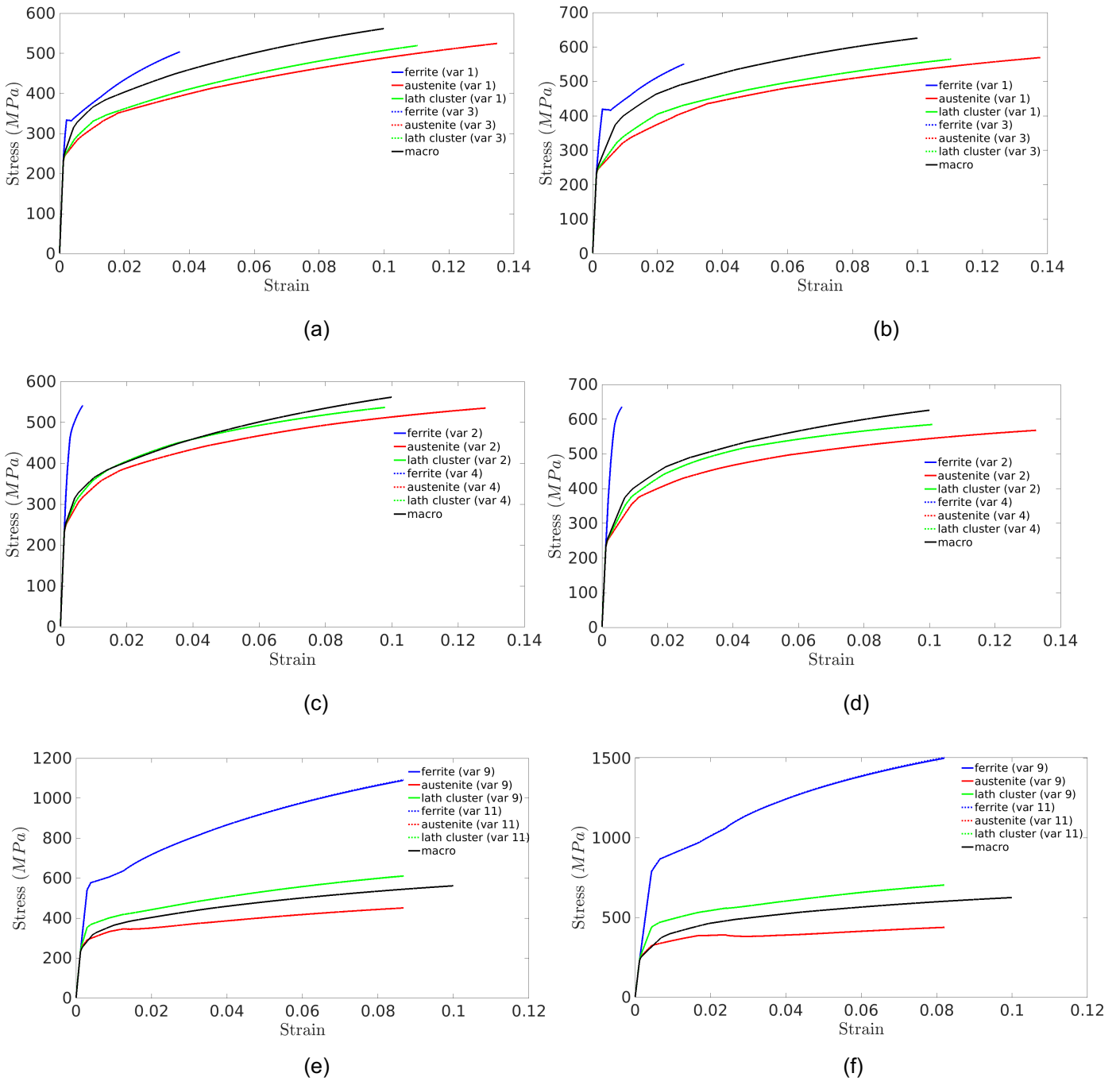
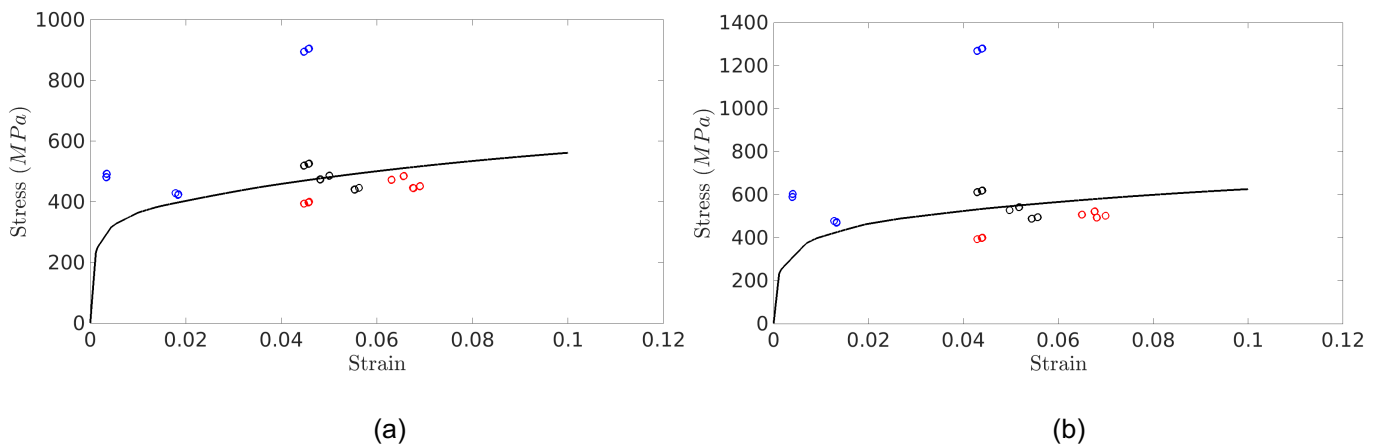


Figure 19. Comparisons between the true stress/true strain responses according to the X-direction obtained for the *first group* with variants 1, 3 (H1, B1): (a) no aging, (b) aging; for the *second group* with variants 2, 4 (H2, B2): (c) no aging, (d) aging; for the *third group* with variants 9, 11 (H5, B2): (e) no aging, (f) aging.

4.6. Multiscale stress and strain heterogeneities

An interesting application of the present three-scale homogenization model is to study multi-scale stress and strain heterogeneities, which is not possible with a simple two-scale homogenization model.

In Figure 20, we report stress/strain states at both micro- and meso-scales recorded at 5% of macroscopic strain, with their component along the tensile direction (X-direction). Two orientations are considered for the single primary ferritic grain: $\phi_1 = 0^\circ, \phi = 0^\circ, \phi_2 = 0^\circ$ (tensile loading along the [100] direction in ferrite frame), see Figures 20(a,b), and: $\phi_1 = 18.11^\circ, \phi = 40.12^\circ, \phi_2 = 7.52^\circ$ in Figures 20(c,d). Figures 20(a,c) correspond to non-aged cases while Figures 20(b,d) correspond to aged ones. For all cases, it is clearly observed that the highest stress and strain heterogeneities are present at the microscale in ferrite (see blue circles). Stress and strain heterogeneities in austenite (see red circles) are always lower than for ferrite. In Figures 20(a,b), three groups of variants are clearly visible to give three different internal mechanical states: one is close to the iso-strain state, while the two others are close to the iso-stress state. As seen in section 4.3, these groups depend on the HP orientation with respect to the loading direction. Stress and strain heterogeneities at the mesoscale (average stresses and strains in lath clusters, see black circles) are much lower in magnitude but are far from specific internal states like iso-strain or iso-stress. This result proves again that a simple Voigt model (iso-strain assumption) is not applicable to derive the mechanical state at the mesoscale. When the orientation of the single primary ferritic grain is changed, Figures 20(c,d) display more stress/strain heterogeneities at micro- and macro-scales due to a larger crystal orientation spread. Such trend looks like polycrystalline non-uniform deformation and stress distributions (see e.g., Nicaise et al., 2011). However, here, two different scales are considered for strain and stress heterogeneities and those in ferrite (at the microscale) remain the largest. Figure 20 shows that for all studied cases, the multiscale modelling and simulations have been truly accomplished and the averaging strain and stress relationships between scales are satisfied.



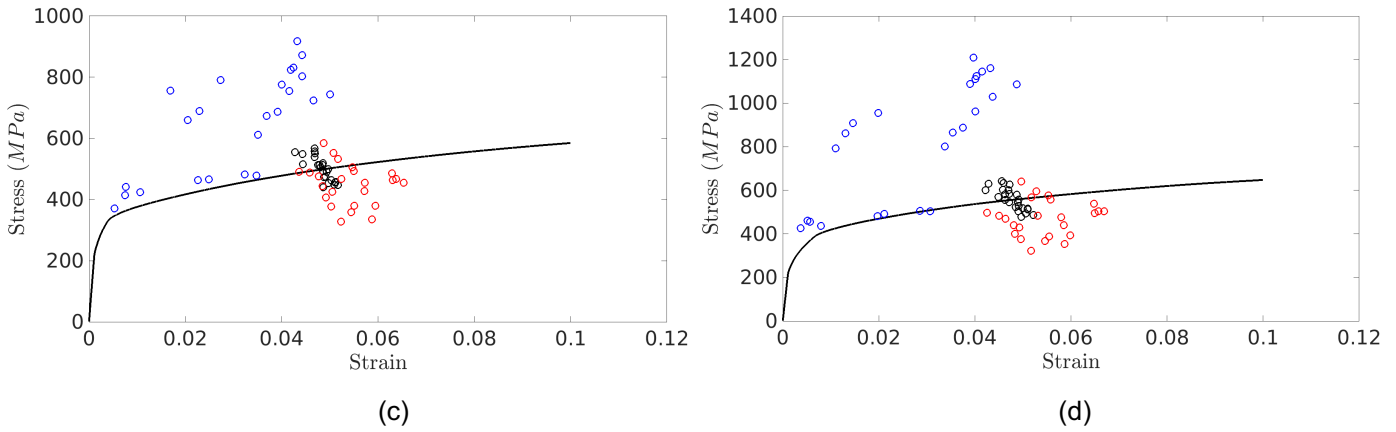


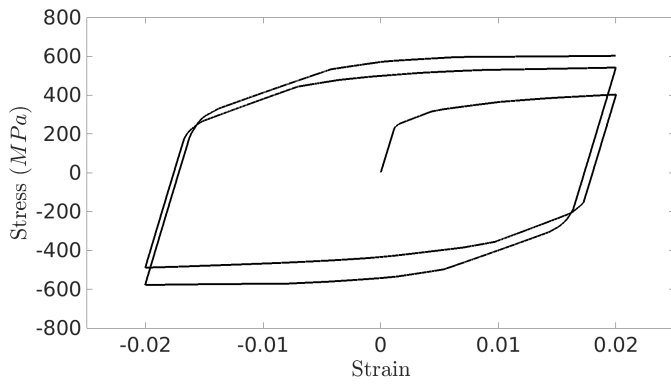
Figure 20. Macroscopic tensile true stress/true strain response (solid line), and, corresponding stress/strain states recorded at the mesoscale (black circles), and, at the microscale for ferrite (blue circles) and for austenite (red circles) at 5% of macroscopic strain. Single primary ferritic grain orientation: $\phi_1 = 0^\circ, \phi = 0^\circ, \phi_2 = 0^\circ$ (a) no aging, (b) aging; Single primary ferritic grain orientation: $\phi_1 = 18.11^\circ, \phi = 40.12^\circ, \phi_2 = 7.52^\circ$ (c) no aging (d) aging.

4.7. Discussion on the Bauschinger effect in the light the three-scale model

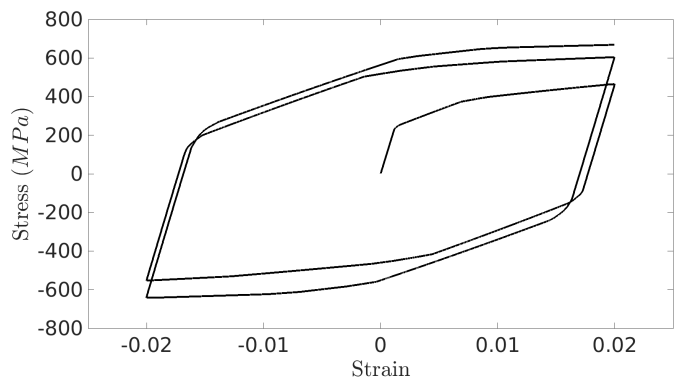
Finally, let us study the respective influences of ferritic grain orientations and aging on internal stress developments during tension-compression, i.e. reverse loading. Polycrystal plasticity models are good candidates to study load reversals and cyclic hardening/softening behaviors (see e.g., Evrard et al., 2010; Wang et al., 2020). In this duplex steel, the development of internal stresses at the different scales is analyzed in the light of the present model to study the Bauschinger effect, which is defined as the difference in plastic flow stress after reversed deformation (Atkinson et al., 1974; Corbin et al., 1996). Such study was investigated in as received and aged duplex stainless steels by Verhaeghe et al. (1996). Even though the Méric-Cailletaud's crystal plasticity model can be used with intra-crystalline kinematical hardening (through calibrating parameters c and d in equation (36)), we have not considered it here, since no experimental cyclic tests were performed to calibrate these parameters on this specific material.

At the mesoscale, the incompatibility stresses are dependent on the HP orientation with respect to the loading direction (see Figure 10), which lead to a backstress originating from inter-phase stress accommodation. Figure 21 reports simulated cyclic responses (2 cycles) performed in tension (forward loading) and compression (reverse loading) for the case of one primary ferritic grain with 24 KS variants (i.e., 24 grains with two-phase LS), and for the case of 15 primary ferritic grains with 24 KS variants in each grain (i.e., 360 grains with two-phase LS). Figures 21(a) and 21(b) compare the cyclic responses with no aging and with aging, respectively, for $\phi_1 = 0^\circ, \phi =$

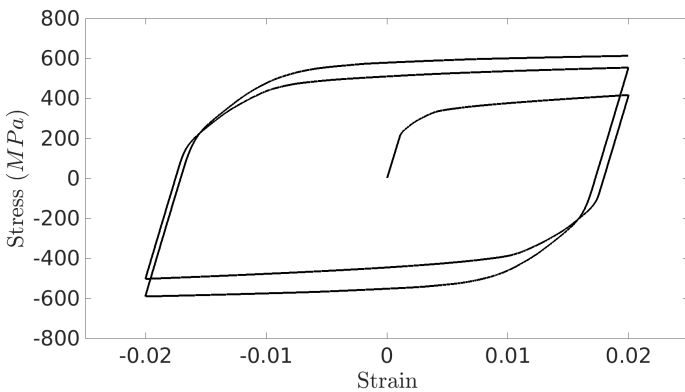
$0^\circ, \phi_2 = 0^\circ$. Figures 21(c) and 21(d) compare the cyclic responses with no aging and with aging, respectively, for $\phi_1 = 18.11^\circ, \phi = 40.12^\circ, \phi_2 = 7.52^\circ$. Figures 21(e) and 21(f) compare the cyclic responses of the case of an ensemble of 15 primary ferritic grains with no aging and with aging, respectively. Following Atkinson et al. (1974), Corbin et al. (1996) and Verhaeghe et al. (1996), the overall backstress at the macroscale (Σ_b) reflecting the Bauschinger effect is defined as $\Sigma_b = (\Sigma_f - \Sigma_r)/2$, where Σ_f is the forward flow stress at 2% of strain and Σ_r is the reverse stress at the onset of plasticity in compression during the first cycle. The results for the simulations are gathered in Table 4. It is shown that the increase in backstress due to aging is important. This increase varies from 51 to 65 MPa, see Figures 21(b)(d)(f). The role of the ferritic grain orientation is highlighted. The cyclic curves in the elastic-plastic transitions are more rounded (see Figure 21(c) compared to Figure 21(a)) due to the larger scatter of internal stresses (see Figures 20(c,d) compared to Figures 20(a,b)), and, the backstress increase is 37 MPa. This phenomenon is even more pronounced for the case of 15 primary ferritic grains, where the backstress increase is equal to 73 MPa between Figure 21(a) and Figure 21(e). It is found that the largest backstress is given for the aged case with 15 primary ferritic grains. These gradual increase of backstress Σ_b for each configuration is due to an increase of stress heterogeneities in both phases when upscaling from the mesoscale to macroscale.



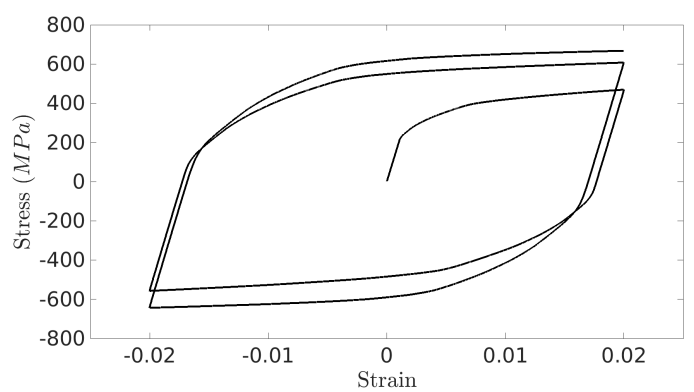
(b)



(b)



(c)



(d)

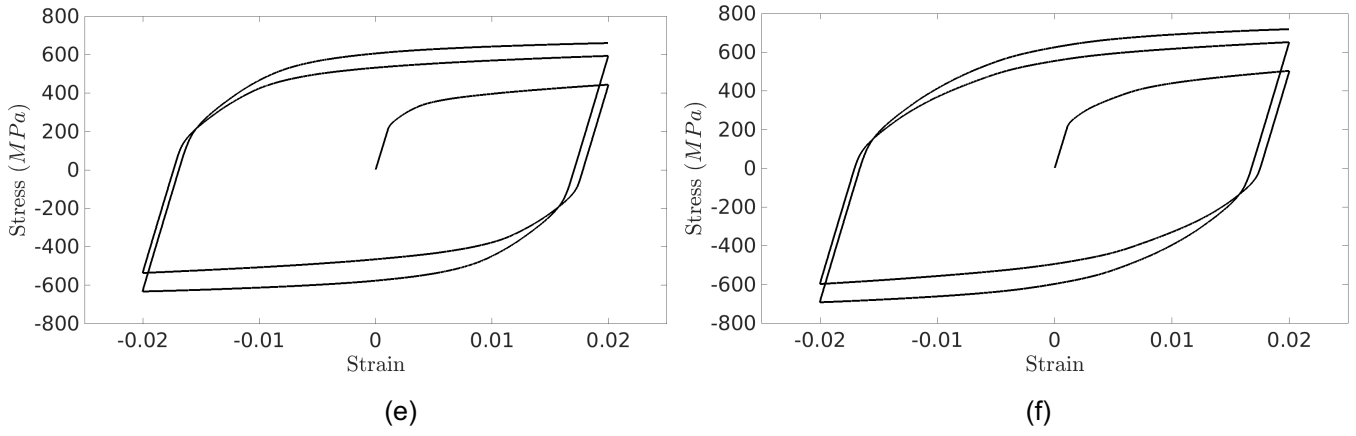


Figure 21. Tension-compression cyclic responses (2 cycles, true stress/true strain curves) for one single primary ferritic grain with orientation: $\phi_1 = 0^\circ, \phi = 0^\circ, \phi_2 = 0^\circ$ (a) no aging, (b) aging; one single primary ferritic grain with orientation given by $\phi_1 = 18.11^\circ, \phi = 40.12^\circ, \phi_2 = 7.52^\circ$ (c) no aging, (d) aging; ensemble of 15 primary ferritic grains: (e) no aging, (f) aging.

Table 4. Values of forward flow stress Σ_f at 2% of strain, Σ_r reverse stress at the onset of plasticity in compression, and backstress Σ_b for the simulations of different microstructures with non-aged or aged condition.

Microstructures and RVEs	Σ_f (MPa)	Σ_r (MPa)	Σ_b (MPa)
One primary ferritic grain RVE: 24 grains with LS $\phi_1 = 0^\circ, \phi = 0^\circ, \phi_2 = 0^\circ$ Non-aged	397	153	122
One primary ferritic grain RVE: 24 grains with LS $\phi_1 = 0^\circ, \phi = 0^\circ, \phi_2 = 0^\circ$ Aged	464	90	187
One primary ferritic grain RVE: 24 grains with LS $\phi_1 = 18.11^\circ, \phi = 40.12^\circ, \phi_2 = 7.52^\circ$ Non-aged	418	100	159
One primary ferritic grain RVE: 24 grains with LS $\phi_1 = 18.11^\circ, \phi = 40.12^\circ, \phi_2 = 7.52^\circ$ Aged	465	45	210
Ensemble of 15 primary ferritic grains RVE: 360 grains with LS Non-aged	439	49	195
Ensemble of 15 primary ferritic grains RVE: 360 grains with LS Aged	503	9	247

5. Conclusions

In this paper, a three-scale microstructure-based elasto-viscoplastic homogenization model is presented for the first time to predict the local and the overall behavior of a CF8M alloy, which is a cast duplex stainless steel used primary loop components of Pressurized Water Reactors (PWR). Mechanical tensile tests have been performed on as received (cast) and aged (1000h, 350°C) alloy to identify the crystal plasticity parameters based on the Méric-Cailletaud (1991a,b)'s model at the level of single austenite laths and ferrite interlayers. The main conclusions of the paper are the following:

- The model is able to describe the average mechanical fields (stress and strain fields) at the different scales of the duplex steel microstructure: (i) in the austenite laths and in the ferrite interlayer related with a KS-OR, (ii) at the level of a cluster of austenite laths in the two-phase LS structure, (iii) at the level of primary ferritic grains, (iv) at the level of an ensemble of primary ferritic grains.
- The morphology due to the cluster of austenite laths is responsible for a strong anisotropic behavior observed from the mechanical responses of LS structure satisfying a pure KS-OR. This trend was confirmed with comparisons with EVPFFT simulations with same crystal plasticity laws. The slip analysis confirms the important effects of incompatibility stresses dependent on the local configuration defined by the HP and the tensile directions. Generally, the individual responses of both phases are not sufficient to represent the stress/strain responses of the LS structure, except for the case where the loading direction is parallel the $[1\ 1\ 1]$ crystallographic direction in ferrite.
- In the case where the tensile loading is performed according to the $[1\ 0\ 0]$ crystallographic direction in ferrite, it is found that the tensile stresses in ferrite strongly depend on the HP orientation with respect to the loading direction, where we have identified three groups of KS variants with similar mechanical behavior. The effect of primary ferritic grain crystallographic orientation is important and changes the internal mechanical state in ferrite for the different variants belonging to the three above identified groups. It was also observed that stress heterogeneities are more pronounced inside the primary ferritic grain.
- The effect of aging was discussed assuming that the microstructure of ferrite has changed, affecting only the intra-granular isotropic hardening parameters of ferrite. These parameters were identified using the tensile stress/strain curve for the aged specimen. Then, aging was

found to enhance the mechanical contrast between both phases and increase the incompatibility stresses.

- Finally, the Bauschinger effect was studied in the light of the model with and without aging for cyclic tension-compression loading for different microstructures. It was shown that the backstress depends on ferritic grain orientation and aging. The largest backstress was found for the aged material constituted of 15 primary ferritic grains constituted of 24 spherical domains with two-phase LS, representing lath clusters in each ferritic grain.

Some interesting research directions remain to do with the present developed three-scale model. First, we will aim to perform some predictions in comparison with *in situ* mechanical tests extracting kinematical strain fields like *in situ* digital image correlation (see e.g. Guéry et al., 2016), high-resolution digital image correlation (HR-DIC) (Harte et al., 2020; Maresca et al., 2020), or, lattice strain evolution in the elastoplastic transition (*in situ* X-Ray diffraction, see e.g. Wang et al., 2016; Gadalinska et al., 2020). Bauschinger tests on cast and aged specimen can be performed to identify kinematical hardening parameters at the single crystalline level. The hydrostatic pressure fields, as predicted by the present three-scale model, as well as slip activities can be used to predict damage initiation during aging. The present model can be applied to other two-phase complex microstructures involving laminate structures like pearlitic steels (Delannay, 2018) or two-phase titanium alloys with Burgers-OR (Fan et al. 2018). Lastly, the present three-scale micromechanical model can be incorporated in structural FE-based calculations using the MFront code generator (Helfer et al. 2015), as performed in Tsekpuia (2022).

Acknowledgments

The authors thank the MAI-SN (Materials Aging Institute – Scientific Network) for financial support. Fruitful discussions with Maxime Mollens (EDF R&D), Stéphane Roux (ENS Paris Saclay) and Lionel Germain (LEM3 Metz) are acknowledged.

Appendix

Appendix A. Crystallographic orientation data

Table A.1. List of the 24 cubic symmetry group matrices used to generate the crystallographic orientations of the 24 KS-OR variants in Table 2.

Variant Number	Cubic symmetry group matrices
V1	$\begin{bmatrix} 1 & 0 & 0 \\ 0 & 1 & 0 \\ 0 & 0 & 1 \end{bmatrix}$
V2	$\begin{bmatrix} 0 & -1 & 0 \\ 1 & 0 & 0 \\ 0 & 0 & 1 \end{bmatrix}$
V3	$\begin{bmatrix} -1 & 0 & 0 \\ 0 & -1 & 0 \\ 0 & 0 & 1 \end{bmatrix}$
V4	$\begin{bmatrix} 0 & 1 & 0 \\ -1 & 0 & 0 \\ 0 & 0 & 1 \end{bmatrix}$
V5	$\begin{bmatrix} 1 & 0 & 0 \\ 0 & 0 & -1 \\ 0 & 1 & 0 \end{bmatrix}$
V6	$\begin{bmatrix} 0 & -1 & 0 \\ 0 & 0 & -1 \\ 1 & 0 & 0 \end{bmatrix}$
V7	$\begin{bmatrix} -1 & 0 & 0 \\ 0 & 0 & -1 \\ 0 & -1 & 0 \end{bmatrix}$
V8	$\begin{bmatrix} 0 & 1 & 0 \\ 0 & 0 & -1 \\ -1 & 0 & 0 \end{bmatrix}$
V9	$\begin{bmatrix} 0 & 0 & 1 \\ 1 & 0 & 0 \\ 0 & 1 & 0 \end{bmatrix}$
V10	$\begin{bmatrix} 0 & 0 & 1 \\ 0 & -1 & 0 \\ 1 & 0 & 0 \end{bmatrix}$
V11	$\begin{bmatrix} 0 & 0 & 1 \\ -1 & 0 & 0 \\ 0 & -1 & 0 \end{bmatrix}$
V12	$\begin{bmatrix} 0 & 0 & 1 \\ 0 & 1 & 0 \\ -1 & 0 & 0 \end{bmatrix}$
V13	$\begin{bmatrix} -1 & 0 & 0 \\ 0 & 0 & 1 \\ 0 & -1 & 0 \end{bmatrix}$
V14	$\begin{bmatrix} 0 & 1 & 0 \\ 0 & 0 & 1 \\ 1 & 0 & 0 \end{bmatrix}$
V15	$\begin{bmatrix} 1 & 0 & 0 \\ 0 & 0 & 1 \\ 0 & -1 & 0 \end{bmatrix}$
V16	$\begin{bmatrix} 0 & -1 & 0 \\ 0 & 0 & 1 \\ -1 & 0 & 0 \end{bmatrix}$

V17	$\begin{bmatrix} 0 & 0 & -1 \\ -1 & 0 & 0 \\ 0 & 1 & 0 \end{bmatrix}$
V18	$\begin{bmatrix} 0 & 0 & -1 \\ 0 & 1 & 0 \\ 1 & 0 & 0 \end{bmatrix}$
V19	$\begin{bmatrix} 0 & 0 & -1 \\ 1 & 0 & 0 \\ 0 & -1 & 0 \end{bmatrix}$
V20	$\begin{bmatrix} 0 & 0 & -1 \\ 0 & -1 & 0 \\ -1 & 0 & 0 \end{bmatrix}$
V21	$\begin{bmatrix} 1 & 0 & 0 \\ 0 & -1 & 0 \\ 0 & 0 & -1 \end{bmatrix}$
V22	$\begin{bmatrix} 0 & 1 & 0 \\ 1 & 0 & 0 \\ 0 & 0 & -1 \end{bmatrix}$
V23	$\begin{bmatrix} -1 & 0 & 0 \\ 0 & 1 & 0 \\ 0 & 0 & -1 \end{bmatrix}$
V24	$\begin{bmatrix} 0 & -1 & 0 \\ -1 & 0 & 0 \\ 0 & 0 & -1 \end{bmatrix}$

Table A.2. Averaged crystallographic orientations (Euler-Bunge angles) of reconstructed ferritic grains from EBSD maps.

Primary ferritic grains	ϕ_1 (°)	ϕ (°)	ϕ_2 (°)
1*	18.11	40.12	7.52
2	25.86	35.40	46.27
3	150.47	9.73	0.61
4	106.38	20.88	75.83
5	140.37	32.08	66.45
6	190.89	44.42	51.02
7	178.52	42.59	28.43
8	195.83	40.65	43.53
9	109.88	36.43	19.41
10	195.21	15.2	40.48
11	353.19	8.85	356.26
12	229.57	41.94	40.62
13	89.43	33.77	60.68
14	177.31	24.8	8.22
15	319.43	39.12	58.27

*: largest grain used for simulation of the single primary ferritic grain.

Appendix B. Detailed components of the 6×6 matrices F_{ij}^c and G_{ij}^s used in the two-phase laminate structure (LS) model

The non-zero components of the 6×6 symmetric matrix F_{ij}^c associated with c_{ij} (6×6 elastic stiffness matrix) is obtained analytically and is given by:

$$\begin{aligned} F_{22}^c &= (c_{44}^* c_{66}^* - c_{46}^{*2})/D & F_{24}^c &= (c_{26}^* c_{46}^* - c_{24}^* c_{66}^*)/D & F_{26}^c &= (c_{24}^* c_{46}^* - c_{26}^* c_{44}^*)/D \\ F_{44}^c &= (c_{22}^* c_{66}^* - c_{15}^{*2})/D & F_{46}^c &= (c_{24}^* c_{26}^* - c_{22}^* c_{46}^*)/D & F_{66}^c &= (c_{22}^* c_{44}^* - c_{24}^{*2})/D \end{aligned} \quad (B.1)$$

with $D = c_{22}^* c_{44}^* c_{66}^* + 2c_{24}^* c_{46}^* c_{26}^* - c_{26}^{*2} c_{44}^* - c_{46}^{*2} c_{22}^* - c_{24}^{*2} c_{66}^*$ and $c_{ij}^* = f^\gamma c_{ij}^\alpha + f^\alpha c_{ij}^\gamma$.

The non-zero components of the 6×6 symmetric matrix G_{ij}^s associated with s_{ij} (6×6 elastic compliance matrix) is obtained analytically and is given by:

$$\begin{aligned} G_{11}^s &= (s_{33}^* s_{55}^* - s_{35}^{*2})/D & G_{13}^s &= (s_{15}^* s_{35}^* - s_{13}^* s_{55}^*)/D & G_{15}^s &= (s_{13}^* s_{35}^* - s_{15}^* s_{33}^*)/D \\ G_{33}^s &= (s_{11}^* s_{55}^* - s_{15}^{*2})/D & G_{35}^s &= (s_{13}^* s_{15}^* - s_{11}^* s_{35}^*)/D & G_{55}^s &= (s_{11}^* s_{33}^* - s_{13}^{*2})/D \end{aligned} \quad (B.2)$$

with $D = s_{11}^* s_{33}^* s_{55}^* + 2s_{13}^* s_{35}^* s_{15}^* - s_{15}^{*2} s_{33}^* - s_{35}^{*2} s_{11}^* - s_{13}^{*2} s_{55}^*$ and $s_{ij}^* = f^\gamma s_{ij}^\alpha + f^\alpha s_{ij}^\gamma$.

Appendix C. Crystallographic slip systems for f.c.c. austenite and b.c.c. ferrite

Table C.1. The 12 slip systems in the f.c.c. structure with Schmid and Boas's notation (1968).

Notation	Crystallographic plane	Crystallographic direction
A2	$(\bar{1} 1 1)$	$[0 \bar{1} 1]$
A3	$(\bar{1} 1 1)$	$[1 0 1]$
A6	$(\bar{1} 1 1)$	$[1 1 0]$
B2	$(1 1 1)$	$[0 \bar{1} 1]$
B4	$(1 1 1)$	$[\bar{1} 0 1]$
B5	$(1 1 1)$	$[\bar{1} 1 0]$
C1	$(\bar{1} \bar{1} 1)$	$[0 1 1]$
C3	$(\bar{1} \bar{1} 1)$	$[1 0 1]$
C5	$(\bar{1} \bar{1} 1)$	$[\bar{1} 1 0]$
D1	$(1 \bar{1} 1)$	$[0 1 1]$
D4	$(1 \bar{1} 1)$	$[\bar{1} 0 1]$
D6	$(1 \bar{1} 1)$	$[1 1 0]$

Table C.2. The 12 slip systems in the b.c.c. structure with their notations according to Le et al. (2020).

Notation	Crystallographic plane	Crystallographic direction
2A	$(0 \bar{1} 1)$	$[\bar{1} 1 1]$
3A	$(1 0 1)$	$[\bar{1} 1 1]$
6A	$(1 1 0)$	$[\bar{1} 1 1]$
2B	$(0 \bar{1} 1)$	$[1 1 1]$
4B	$(\bar{1} 0 1)$	$[1 1 1]$
5B	$(\bar{1} 1 0)$	$[1 1 1]$
1C	$(0 1 1)$	$[\bar{1} \bar{1} 1]$
3C	$(1 0 1)$	$[\bar{1} \bar{1} 1]$
5C	$(\bar{1} 1 0)$	$[\bar{1} \bar{1} 1]$
1D	$(0 1 1)$	$[1 \bar{1} 1]$
4D	$(\bar{1} 0 1)$	$[1 \bar{1} 1]$
6D	$(1 1 0)$	$[1 \bar{1} 1]$

References

- Atkinson, J.D., Brown, L.M., Stobbs, W.M., 1974. The work-hardening of copper-silica. IV. The Bauschinger effect and plastic relaxation, *Philos. Mag.* 30, 1247-1280 (doi: doi.org/10.1080/14786437408207280)
- Auger, P., Danoix, F., Menand, A., Bonnet, S., Bourgoïn, J., Guttman, M., 1990. Atom probe and transmission electron microscopy study of aging of cast duplex stainless steels. *Mater. Sci. Tech.* 6(3), 301-313, 1743-2847 (doi: 10.1179/mst.1990.6.3.301)
- Baczmański, A., Zhao, Y., Gadalińska, E., Le Joncour, L., Wronski, S., Braham, C., Panicaud, B., François, M., Buslaps, T., Soloduha, K., 2016. Elastoplastic deformation and damage process in duplex stainless steels studied using synchrotron and neutron diffractions in comparison with a self-consistent model, *Int. J. Plast.* 81, 102-122. (doi: 10.1016/j.ijplas.2016.01.018)
- Badyka, R., Monnet, G., SAILLET, S., Domain, C., Pareige, C., 2019. Quantification of hardening contribution of G-Phase precipitation and spinodal decomposition in aged duplex stainless steel: APT analysis and micro-hardness measurements, *J. Nucl. Mater.* 514, 266-275 (doi: 10.1016/j.jnucmat.2018.12.002)
- Berbenni, S., Capolungo, L., 2015. A Mori-Tanaka homogenization scheme for non-linear elasto-viscoplastic heterogeneous materials based on Translated Fields: an “affine” extension. *Comptes Rendus de Mécanique* 343, 95-106 (doi: 10.1016/j.crme.2014.12.003)
- Berbenni, S., Paliwal, B., Cherkaoui, M., 2013. A micromechanics-based model for shear-coupled grain boundary migration in bicrystals. *Int. J. Plast.* 44, 68-94 (doi: 10.1016/j.ijplas.2012.11.011)
- Berbenni, S., Taupin, V., Lebensohn, R. A., 2020. A fast Fourier transform-based mesoscale field dislocation mechanics study of grain size effects and reversible plasticity in polycrystals. *J. Mech. Phys. Solids* 135, 103808 (doi: 10.1016/j.jmps.2019.103808)
- Berbenni, S., 2021. A time-incremental homogenization method for elasto-viscoplastic particulate composites based on a modified secant formulation *Int. J. Solids Struct.* 229,111136 (doi: 10.1016/j.ijsolstr.2021.111136)
- Berveiller, M., Zaoui, A., 1979. An extension of the self-consistent scheme to plastically-flowing polycrystals. *J. Mech. Phys. Solids* 26, 325-344 (doi: 10.1016/0022-5096(78)90003-0)

Bethmont, M., Meyzaud, Y., Soulat, P., 1996. Properties of cast austenitic materials for light water reactors. *Fracture in Austenitic Components*, 65(3):221–229 (doi: 10.1016/0308-0161(94)00133-4)

Bonnet, S., Bourgoïn, J., Champredonde, J., Guttman, D., Guttman, M., 1990. Relationship between evolution of mechanical properties of various cast duplex stainless steels and metallurgical and aging parameters: outline of current EDF programmes. *Mater. Sci. Tech.* 6(3), 221–229 (doi: 10.1179/mst.1990.6.3.221)

Brassard, L., Stainier, L., Doghri, I., Delannay, L., 2012. Homogenization of elasto(visco)plastic composites based on an incremental variational principle. *Int. J. Plast.* 36, 86-112 (doi : 10.1016/j.ijplas.2012.03.010)

Bugat, S., 2000. Comportement et endommagement des aciers austéno-ferritiques vieillis : une approche micromécanique. Ph.D. thesis. Ecole Nationale Supérieure des Mines de Paris, France.

Bugat, S., Besson, J., Pineau, A. 1999. Micromechanical modeling of the behavior of duplex stainless steels. *Comp. Mater. Sci.* 16, 158-166 (doi :10.1016/S0927-0256(99)00058-0)

Bugat, S., Besson, J., Gourgues, A. F., N'Guyen, F., Pineau, A., 2001. Microstructure and damage initiation in duplex stainless steels. *Mater. Sci. Eng. A* 317, 32-36 (doi : 10.1016/S0921-5093(01)01196-0)

Cailletaud, G., Pilvin, P., 1994. Utilisation de modèles polycristallins pour le calcul éléments finis. *Revue Européennes des Éléments Finis* 3(4), 515-541 (doi: 10.1080/12506559.1994.10511147)

Cailletaud, G., 1992. A micromechanical approach to inelastic behavior of metals. *Int. J. Plast.* 8, 55-73 (doi: 10.1016/0749-6419(92)90038-E)

Charles, J., 2009. Corrosion Resistance Properties. In *Duplex Stainless Steels*, pages 47–114. John Wiley & Sons, Ltd. ISBN 978-1-118-55799-0 (doi: 10.1002/9781118557990.ch2)

Corbin, S.F., Wilkinson, D.S., Embury, J.D. 1996. The Bauschinger effect in a particulate reinforced Al alloy, *Mater. Sci. Eng. A* 207, 1-11 (doi: 10.1016/0921-5093(95)10028-8)

Coudon, F., Cailletaud, G., Cormier, J., Marcin, L., 2019. A multiscale model for nickel-based directionally solidified materials. *Int. J. Plast.* 115, 1-17 (doi: 10.1016/j.ijplas.2018.10.003).

- Das, S., Ponte Castañeda, P., 2021. Differential variational estimates for the macroscopic response and field statistics of elasto-viscoplastic polycrystals. *J. Mech. Phys. Solids* 147, 104202 (doi: 10.1016/j.jmps.2020.104202).
- Delannay, L., 2018. Modeling of microscopic strain heterogeneity during wire drawing of pearlite. *Proc. Manufact.* 15, 1893-1899 (10.1016/j.promfg.2018.07.199).
- Devillers-Guerville, L., 1998. Rupture d'aciers inoxydables austéno-ferritiques moulés, fragilisés par vieillissement à 350-400°C: aspects microstructuraux – simulation numérique de la dispersion et des effets d'échelle. Ph.D. thesis, Ecole Nationale Supérieure des Mines de Paris.
- Djaka, K.S., Berbenni, S., Taupin, V., Lebensohn, R. A., 2020. A FFT-based numerical implementation of mesoscale field dislocation mechanics: Application to two-phase laminates. *Int. J. Solids Struct.* 184, 136-152 (doi:10.1016/j.ijsolstr.2018.12.027)
- Dodla, S., Bertram, A., Krüger, M., 2015. Finite element simulation of lamellar copper-silver composites. *Comput. Mater. Sci.* 101, 29-38 (doi:10.1016/j.commatsci.2015.01.012)
- Doghri, I., Adam, L., Bilger, N., 2010. Mean-field homogenization of elasto-viscoplastic composites based on a general incrementally affine linearization method. *Int. J. Plast.* 26, 219-223 (doi: 10.1016/j.ijplas.2009.06.003)
- El Omri, A., Fennan, A., Sidoroff, F., Hihl, A. 2000. Elastic-plastic homogenization for layered composites. *Eur. J. Mech. A/Solids* 19, 585-601 (doi: 10.1016/S0997-7538(00)00182-0)
- Eshelby, J.D., 1957. The determination of the elastic field of an ellipsoidal inclusion, and related problems. *Proc. R. Soc. Lond. Math. Phys. Eng. Sci.* 241, 376-396 (doi: 10.1098/rspa.1957.0133)
- Evrard, P., Aubin, V., Pilvin, P., Degallaix, S., Kondo, D., 2008. Implementation and validation of a polycrystalline model for a bi-phased steel under non-proportional loading paths. *Mech. Res. Comm.* 35, 336-343 (doi: 10.1016/j.mechrescom.2008.01.006)
- Evrard, P., Alvarez-Armas, I., Aubin, V., Degallaix, S., 2010. Polycrystalline modeling of the cyclic hardening/softening behavior of an austenitic-ferritic stainless steel. *Mech. Mater.* 42, 395-404 (doi: 10.1016/j.mechmat.2010.01.007)

Fan, X. G., Jiang, X. Q., Zeng, X., Shi, Y.G., Gao, P.F., Zhan, M., 2018. Modeling the anisotropy of hot plastic deformation of two-phase titanium alloys with a colony microstructure. *Int. J. Plast.* 104, 173-195 (doi: 10.1016/j.ijplas.2018.02.010).

Flipon, B., Keller, C., Quey, R., Barbe, F. 2020. A full-field crystal-plasticity analysis of bimodal polycrystals. *Int. J. Solids Struct.* 184, 178-192 (doi: 10.1016/j.ijsolstr.2019.02.005)

Fournier, B., Sauzay, M., Pineau, A., 2011. Micromechanical model of the high temperature cyclic behavior of 9-12%Cr martensitic steels. *Int. J. Plast.* 27, 1803-1816 (doi:10.1016/j.ijplas.2011.05.007)

Franciosi, P., Berbenni, S., 2007. Heterogeneous crystal and poly-crystal plasticity modeling from a Transformation Field Analysis within a regularized Schmid law. *J. Mech. Phys. Solids* 55, 2265-2299 (doi:10.1016/j.jmps.2007.04.012)

Franciosi, P., Berbenni, S., 2008. Multi-laminate plastic-strain organization for non-uniform TFA modeling of poly-crystal regularized plastic flow. *Int. J. Plast.* 24, 1549-1580 (doi: 10.1016/j.ijplas.2007.12.004)

Franciosi, P., 2020. Multiple continuity of phases in composite materials: overall property and estimates from a laminate system scheme. *Int. J. Solids Struct.* 184, 40-62 (doi: 10/1016/J.ijsolstr.2019.02.021)

Gadalinska, E., Baczanski, A., Braham, C., Gonzalez, G., Sidhom, H., Wronski, S., Buslaps, T., Wierbanowski, K., 2020. Stress localisation in lamellar cementite and ferrite during elastoplastic deformation of pearlitic steel studied using diffraction and modelling. *Int. J. Plast.* 127, 102651 (doi: 10.1016/j.ijplas.2019.102651)

Guery, A., Hild, F., Latourte, F., Roux, S., 2016. Slip activities in polycrystals determined by coupling DIC measurements with crystal plasticity calculations. *Int. J. Plast.* 81, 249-266 (doi: 10.1016/j.ijplas.2016.01.008)

Haghdadi, N., Cizek, P., Hodgson, P.D., Tari, V., Rohrer, G.S., Beladi, H., 2018. Effect of ferrite-to-austenite phase transformation path on the interface crystallographic character distributions in a duplex stainless steel. *Acta Mater.* 145, 196-209 (doi: 10.1016/j.actamat.2017.11.057)

Harte, A., Atkinson, M., Preuss, M., Quinta da Fonseca, J., 2020. A statistical study of the relationship between plastic strain and lattice misorientation on the surface of a deformed Ni-based superalloy. *Acta Mater.* 195, 555-570 (doi: 10.1016/j.actamat.2020.05.029)

Helfer, T., Michel, B., Proix, J.-M., Salvo M., Sercombe, J., Casella, M., 2015. Introducing the open-source MFront code generator: Application to mechanical behaviours and material knowledge management within the PLEIADES fuel element modelling platform. *Comp. Math. Appl.* 70(5), 994-1023 (doi: 10.1016/j.camwa.2015.06.027).

Hill, R., 1965. Continuum micro-mechanics of elastoplastic polycrystals. *J. Mech. Phys. Solids* 13, 89-101 (doi: 10.1016/0022-5096(65)90023-2)

Jeong, Y., Tomé, C.N., 2020. An efficient elasto-visco-plastic self-consistent formulation: Application to steel subjected to loading path changes. *Int. J. Plast.* 135, 102812 (doi: 10.1016/j.ijplas.2020.102812)

Kasemer, M., Dawson, P., 2020. A finite element methodology to incorporate kinematic activation of discrete deformation twins in a crystal plasticity framework. *Comp. Methods Appl. Mech. Engrg.* 358, 112653 (doi: 10.1016/j.cma.2019.112653)

Kowalczyk-Gajewska K. 2011. Micromechanical model of polycrystalline materials with lamellar substructure. *Arch. Metal. Mater.* 56(2), 509-522 (doi: 10.2478/v10172-011-0055-3)

Kröner, E., 1990. Modified green functions in the theory of heterogeneous and/or anisotropic linearly elastic media. In: Weng, G.J., Taya, M., Abé, H. (Eds.), *Micromechanics and Inhomogeneity: the Toshio Mura 65th Anniversary Volume*. Springer New York, New York, NY, pp. 197-211. (doi: 10.1007/978-1-4613-8919-4_13)

Lahellec, N., Suquet, P., 2007. On the effective behavior of non linear inelastic composites: I. Incremental variational principles. *J. Mech. Phys. Solids* 55, 1932-1963 (doi: 10.1016/j.jmps.2007.02.003)

Lahellec, N., Suquet, P., 2013. Effective response and field statistics in elasto-plastic and elasto-viscoplastic composites under radial and non radial loadings. *Int. J. Plast.* 42, 1-30. (doi: 10.1016/j.ijplas.2012.09.005)

Lhadi S., Berbenni, S., Gey, N., Richeton, T., Germain, L., 2018. Micromechanical modeling of the effect of elastic and plastic anisotropies on the mechanical behavior of β -Ti alloys, *Int. J. Plast.* 109, 88-107 (doi: 10.1016/j.ijplas.2018.05.010)

Lhadi, S., Purushottam raj purohit, R. R. P., Richeton, T., Gey, N., Berbenni, S., Perroud, O., Germain, L. 2020. Elasto-viscoplastic tensile behavior of as-forged Ti-1023 alloy: Experiments and micromechanical modeling. *Mater. Sci. Eng. A* 787, 139491 (doi: doi.org/10.1016/j.msea.2020.13949)

Lebensohn, R.A., Canova, G.R., 1997. A self-consistent approach for modelling texture development of two-phase polycrystals: application to titanium alloys. *Acta Mater.* 45 (9), 3687-3694 (doi: 10.1016/S1359-6454(97)00067-0)

Lebensohn, R.A., 1999. Modelling the role of local correlations in polycrystal plasticity using viscoplastic self-consistent schemes. *Modell. Simul. Mater. Sci. Eng.* 7, 739-746 (doi.org/10.1088/0965-0393/7/5/306)

Lebensohn, R.A., Kanjarla, A.K., Eisenlohr, P., 2012. An elasto-viscoplastic formulation based on fast Fourier transforms for the prediction of micromechanical fields in polycrystalline materials. *Int. J. Plast.* 32-33, 59-69 (doi.org/10.1016/j.ijplas.2011.12.005)

Le, L.T., Ammar, K., Forest, S., 2020. Efficient simulation of single and poly-crystal plasticity based on the pencil glide mechanism. *C. R. Méca.* 348 (10-11), 847-876 (doi: 10.5802/crmeca.44)

Le Delliou, P., SAILLET, S., 2015. Integrity and Life Assessment of Cast Duplex Stainless Steel Elbows of EDF PWR Main Coolant Piping. In : Volume 7: Operations, Applications and Components, page V007T07A014. American Society of Mechanical Engineers, Boston, Massachusetts, USA (doi: 10.1115/PVP2015-45231)

Li, J., Romero, I., Segurado, J., 2019. Development of a thermo-mechanically coupled crystal plasticity modeling framework: Application to polycrystalline homogenization. *Int. J. Plast.* 119, 313-330 (doi : 10.1016/j.ijplas.2019.04.008)

Magnin, T., Moret, F., 1982. Mechanical twinning in ferritic stainless steels. *Scripta Metall.*, 16(11), 1225-1228 (doi: 10.1016/0036-9748(82) 90471-9)

- Mareau, C., Berbenni, S., 2015. An affine formulation for the self-consistent modeling of elasto-viscoplastic heterogeneous materials based on the translated field method. *Int. J. Plast.* 64, 134-150 (doi: 10.1016/j.ijplas.2014.08.011)
- Maresca, F., Kouznetsova, V.G., Geers, M.G.D., 2014. Subgrain lath martensite mechanics: A numerical-experimental analysis. *J. Mech. Phys. Solids* 73, 69-83 (doi: 10.1016/j.jmps.2014.09.002)
- Maresca, F., Polatidis, E., Smíd, M., Van Swygenhoven H., Curtin, W. A., 2020. Measurement and prediction of the transformation strain that controls ductility and toughness in advanced steels. *Acta Mater.* 200, 246-255 (doi: 10.1016/j.actamat.2020.08.028).
- Masson, R., Bornert, M., Suquet, P., Zaoui, A., 2000. Affine formulation for the prediction of the effective properties of nonlinear composites and polycrystals. *J. Mech. Phys. Solids* 48, 1203-1227 (doi: 10.1016/S0022-5096(99)00071-X)
- Masson, R., Seck, M.E.B., Fauque, J., Garajeu, M., 2020. A modified secant formulation to predict the overall behavior of elasto-viscoplastic particulate composites. *J. Mech. Phys. Solids* 137, 103874 (doi: 10.1016/j.jmps.2020.103874)
- M'Cirdi, L., 2000. Comportement et endommagement sous sollicitation mécanique d'un acier austéno-ferritique moulé vieilli. Ph.D. thesis. Ecole Nationale Supérieure d'Arts et Métiers, Paris, France.
- M'Cirdi, L., Lebrun, J.L., Inal, K., Barbier, G., 2001. Experimental approach of a crystallographic cleavage criterion in a cast aged duplex stainless steel. *Acta Mater.* 49, 3879-3887 (doi : 10.1016/S1359-6454(01)00249-X)
- Mercier, S., Molinari, A., Berbenni, S., Berveiller, M., 2012. Comparison of different homogenization approaches for elastic-viscoplastic materials. *Modell. Simul. Mater. Sci. Eng.* 20, 024004 (doi: 10.1088/0965-0393/20/2/024004)
- Mercier, S., Molinari, A., 2009. Homogenization of elastic-viscoplastic heterogeneous materials: self-consistent and Mori-Tanaka schemes. *Int. J. Plast.* 25, 1024-1048 (doi: 10.1016/j.ijplas.2008.08.006).
- Méric, L., Cailletaud, G., 1991a. Single crystal modeling for structural calculations: Part 1 - Model presentation. *ASME J. Eng. Mater. Tech.* 113, 162-170 (doi: 10.1115/1.2903374)

- Méric, L., Cailletaud, G., 1991b. Single crystal modeling for structural calculations: Part 2 - Finite element implementation. *ASME J. Eng. Mater. Tech.* 113, 171-182 (doi :10.1115/1.2903375)
- Michaud, W.F., Toben, P.T., Soppet, W. K., Chopra, O.K., 1994. Tensile Property Characterization of Thermally Aged Cast Stainless Steels. Technical Report. NUREG/CR-6142, ANL-93/35.
- Molinari, A., Ahzi, S., Kouddane, R., 1997. On the self-consistent modeling of elastic-plastic behavior of polycrystals. *Mech. Mater.* 26, 43-62 (doi.org/10.1016/S0167-6636(97)00017-3)
- Mollens, M., 2022a. Modélisation multi-échelle du comportement mécanique d'un acier austéno-ferritique vieilli thermiquement. PhD thesis. Ecole Normale Supérieure Paris, Saclay, France.
- Mollens, M., Roux, S., Hild, F., Guery, A., 2022b. Insights into a dualphase steel microstructure using EBSD and image-processing-based workflow. *J. Appl. Crystal.* 55(3), 601-610. (doi: 10.1107/S1600576722004265)
- Mollens, M., Guery, A., Loizard, D., Hild, F., Roux, S., 2022c. Link between BCC-FCC orientation relationship and austenite morphology in CF8M stainless steel. Submitted.
- Nicaise, N., Berbenni, S., Wagner, F., Berveiller, M., Lemoine, X., 2011. Coupled effects of grain size distributions and crystallographic textures on the plastic behaviour of IF steels. *Int. J. Plast.* 27 (2011) 232-249 (doi : 10.1016/j.ijplas.2010.05.001)
- Nye, J.F., 1957. Physical properties of crystals. Clarendon Press, Oxford.
- Paquin, A., Sabar, H., Berveiller, M., 1999. Integral formulation and self-consistent modelling of elasto-viscoplastic behavior of heterogeneous materials. *Arch. Appl. Mech.* 69, 14-35 (doi: 10.1007/s004190050201).
- Paquin, A., Berbenni, S., Favier, V., Lemoine, X., Berveiller, M, 2001. Micromechanical modeling of the elastic-viscoplastic behavior of polycrystalline steels. *Int. J. Plast.* 17, 1267-1302 (doi: 10.1016/S0749-6419(00)00047-4)
- Pareige, C., Emo, J., SAILLET, S., Domain, C., Pareige, P., 2015. Kinetics of G-phase precipitation and spinodal decomposition in very long aged ferrite of a Mo-free duplex stainless steel. *J. Nucl. Mater.* 465, 383-389 (doi: 10.1016/j.jnucmat.2015.06.017)
- Qu, J., Cherkaoui, M., 2006. Fundamentals of micromechanics of solids. John Wiley & Sons, 2006.

Richeton, T., Berbenni, S., 2013. Effects of heterogeneous elasticity coupled to plasticity on stresses and lattice rotations in bicrystals: A Field Dislocation Mechanics viewpoint. *Eur. J. Mech. A/Solids* 3, 231-247 (doi: 10.1016/j.euromechsol.2012.06.010)

Richeton, T., 2022. Stress partitioning and effective behavior of N-phase laminates in anisotropic elasticity from a fast explicit method. *J. Theor. Comp. Appl. Mech.*, March 2022. (doi:10.46298/jtcam.8506)

Riyad, I.A., Feather, W.G., Vasilev, E., Lebensohn, R., McWilliams, B.A., Pilchak, A.L., Knezevic, M., 2021. Modeling the role of local crystallographic correlations in microstructures of Ti-6Al-4V using a correlated structure visco-plastic self-consistent polycrystal plasticity formulation. *Acta Mater.* 203, 116502 (doi: 10.1016/j.actamat.2020.116502).

Roos, A., Chaboche, J.-L., Gélébart, L., Crépin, J., 2004. Multiscale modelling of titanium aluminides. *Int. J. Plast.* 20, 811-830 (doi: 10.1016/j.ijplas.2003.08.005)

Roters, F., Eisenlohr, P., Hantcherli, L., Tjahjanto, D. D., Bieler, T.R., Raabe, D., 2010. Overview of constitutive laws, kinematics, homogenization and multiscale methods in crystal plasticity finite-element modeling: Theory, experiments, applications. *Acta Mater.* 58 (2010) 1152-1211 (doi: 10.1016/j.actamat.2009.10.058)

Schmid, E., Boas, W. 1968. *Plasticity of crystals with special reference to metals.* Chapman & Hall.

Sigmund, T., Werner, E., Fischer, F.D., 1995. On the thermomechanical deformation behavior of duplex-type materials. *J. Mech. Phys. Solids* 43, 495-532 (doi: 10.1016/0022-5096(95)00003-2)

Solomon, H.D., Devine, T.M., 1982. *Duplex stainless steels: a tale of two phases.* American Society for Metals.

Song, P., Ji, Y., Chen, L., Liu, W., Zhang, C., Chen, L.Q., Zhigang, Y., 2016. Phase-field simulation of austenite growth behavior: Insights into the austenite memory phenomenon. *Comp. Mater. Sci.* 117, 139-150 (doi: 10.1016/j.commatsci.2016.01.030)

Stupkiewicz, S., Petryk, H., 2002. Modelling of laminated microstructures in stress-induced martensitic transformations. *J. Mech. Phys. Solids* 50, 2303-2331 (doi: 10.1016/S0022-5096(02)00029-7)

Taylor, G.I., 1938. Plastic strain in metals. *J. Inst. Metals* 61, 307–324.

Tiba, I., Richeton, T., Motz, C., Vehoff, H., Berbenni, S., 2015. Incompatibility stresses at grain boundaries in Ni bicrystalline micropillars analyzed by an anisotropic model and slip activity. *Acta Mater.* 83, 227-238 (doi: 10.1016/j.actamat.2014.09.033)

Trautwein, A., Gysel, W., 1982. Influence of Long-Time Aging of CF8 and CF8M Cast Steel at Temperatures Between 300 and 500°C on Impact Toughness and Structural Properties. In *Stainless Steel Castings*, pages 165–165–25. ASTM International, 100 Barr Harbor Drive, PO Box C700, West Conshohocken, PA 19428-2959 (doi: 10.1520/STP28441S).

Tsekpuia, E., 2022. Développement et implémentation numérique d'un modèle d'homogénéisation élastoviscoplastique à base microstructurale pour des aciers inoxydables austénito-ferritiques. PhD thesis. Université de Lorraine, Metz, France.

Uchida, M., Tada, N., 2013. Micro-, meso- to macroscopic modeling of deformation behavior of semi-crystalline polymer. *Int. J. Plast.* 49, 164-184 (doi: 10.1016/j.ijplas.2013.03.007).

Verhaeghe, B., Bréchet, Y., Louchet, F., Massoud, J.P., Touzeau, D., 1996. Internal stresses in an austenoferritic duplex stainless steel. *Phys. Stat. Sol. (a)* 153, 47-56 (doi: doi.org/10.1002/pssa.2211530104)

Verhaeghe, B., Louchet, F., Bréchet, Y., Massoud, J.-P., 1997. Damage and rupture mechanisms in an austenoferritic duplex steel. *Acta Mater* 45(5):1811-1819 (doi: 10.1016/S1359-6454(96)00330-8)

Wang, H., Wu, P.D., Tomé, C.N., Huang, Y., 2010. A finite strain elastic-viscoplastic self-consistent model for polycrystalline materials. *J. Mech. Phys. Solids* 58, 594-612 (doi: 10.1016/j.jmps.2010.01.004)

Wang, H., Clausen, B., Capolungo, L., Beyerlein, I.J., Wang, J., Tomé, C.N., 2016. Stress and strain relaxation in magnesium AZ31 rolled plate: In-situ neutron measurement and elastic viscoplastic polycrystal modeling. *Int. J. Plast.* 79, 275-292 (doi: 10.1016/j.ijplas.2015.07.004)

Wang, J., Zecevic, M., Knezevic, M., Beyerlein, I. J., 2020. Polycrystal plasticity modeling for load reversals in commercially pure titanium. *International Journal of Plasticity* 125, 294-313 (doi: 10.1016/j.ijplas.2019.09.013)

Weng, G.J., 1990. The overall elastoplastic stress-strain relations of dual-phase metals. *J. Mech. Phys. Solids* 38, 419-441 (doi: 10.1016/0022-5096(90)90007-Q)

Wu, L., Adam, L., Doghri, I., Noels, L., 2017. An incremental-secant mean field homogenization method with second statistical moments for elasto-viscoplastic composite materials. *Mech. Mater.* 114, 180-200 (doi: 10.1016/j.mechmat.2017.08.006)

Zecevic, M., Lebensohn, R. A., 2020. New robust self-consistent homogenization schemes of elasto-viscoplastic polycrystals. *Int. J. Solids Struct.* 202, 434-453 (doi:10.1016/j.ijsolstr.2020.05.032)